Light-Scattering in Strongly Scattering Media - Multiple-Scattering and Weak Localization

Vandermark, M.B.; Vanalbada, M.P.; Lagendijk, A.

DOI
10.1103/PhysRevB.37.3575

Publication date
1988

Published in
Physical Review. B, Condensed Matter

Light scattering in strongly scattering media: Multiple scattering and weak localization

Martin B. van der Mark, Meint P. van Albada, and Ad Lagendijk
Natuurkundig Laboratorium der Universiteit van Amsterdam, Valckenierstraat 65, 1018 XE Amsterdam, The Netherlands
(Received 27 April 1987)

Recently the interest in interference effects in multiple (elastic) scattering of waves has undergone an important revival due to the discovered connection with Anderson localization. In this paper we discuss a rigorous scalar wave theory as a model to represent the enhanced backscattering (weak localization) of light for finite slabs. In addition, we discuss a general theory based on a diffusion approximation, and the resulting angular-dependent enhanced backscattering intensity will be presented in closed form for finite slabs and for general albedo. New transmission and reflection experiments for strongly scattering media are presented. Two types of liquid suspensions have been used as study object: polystyrene spheres in water and suspensions of TiO_2 particles in 2-methylpentane-2,4-diol. From these experiments scattering mean free paths and transport mean free paths have been obtained. Relative values for the transport mean free paths could also independently be inferred from the observation of the angular dependence of enhanced (interference) backscattering. The observed shapes and widths of the enhanced backscattering cones are in very good agreement with the calculated values. A less satisfying feature is that the theory predicts a backscattering intensity of twice the background intensity, while the experimental value is some 15–20 % lower.

I. INTRODUCTION

Recently the connection between multiple elastic scattering and the possibility of localization of *waves*, on the one hand, and Anderson localization of *electrons*, on the other hand, has attracted a great deal of attention.[1–9] The experimental observation of weak localization of light[10–15] has brought these discussions on a more realistic level. Essentially weak localization of light is the phenomenon of enhanced backscattering from a random medium due to interference effects which occur over distances much larger than the mean free path.[13,16,17] The connection with universal conductance theories[18,19] of electrons has been pointed out.[12,14,20]

Much insight in the field of multiple light scattering has already been gathered, but some results may have escaped the attention of workers in the field of weak localization of waves, because most results have been communicated in either astrophysical literature or in more technical journals. Characteristics of multiple light scattering like attenuation, depolarization, anisotropy, etc., are of essential importance in understanding the radiation field in an atmosphere.[21] Even effects as enhanced backscattering have been known in the astrophysical community (*Gegenschein* or opposition effect),[22,23] although different explanations, not involving interference, have been put forward. Excellent books on (multiple) light scattering have been published.[24–28]

From the theoretical side a theory is needed which describes the occurrence of weak localization of light in a finite slab. Two basic simplifications are usually made: (i) supposition of isotropic scalar scattering and (ii) assumption that the scattering can be described with a diffusion equation. We have relaxed one of these approximations by not resorting to the diffusion approximation. The theory we developed is essentially a rigorous simplification of the work of Tsang ad Ishimaru.[16] Through this simplification we can handle slab widths up to 32 mean free paths with albedo equal to one without numerical problems. Our theory is an isotropic scalar scattering theory, which means that it can only be used for the experimental results in which incident and detected polarization are parallel. Recently Stephen and Cwillich have treated the phenomenon of weak localization of *vector* waves in the Rayleigh limit; however, they relied on the diffusion approximation.[29] Akkermans *et al.* have introduced a diffusion approximation for a semi-infinite slab and conservative scattering (albedo of 1).[17] We will present an extension of the diffusion approach here to include finite slabs and nonconservative scattering in closed form. This theory will be compared with the rigorous theory. This is important in view of the fact that the observation of the breakdown of diffusion theory for thick slabs (Anderson localization) will very likely involve the study of finite size effects of the sample.

In all the recent reflections on localization of waves key parameters are the scattering mean free path λ_{sc} (defined as the reciprocal of the turbidity) and transport mean free path λ_{tr}. In this paper we report on systematic studies of these parameters. Our random media are suspensions of dielectric particles in a liquid. Two types of suspensions have been studied in detail: polystyrene spheres in water and rutile particles in 2-methylpentane-2,4-diol. Our experiments consist of detection of elastically scattered radiation both at and in the neighborhood of the forward and the backward directions. In the backward direction one observes an enhancement due to constructive interference, a phenomenon which is now known as weak localization of light. Parameters which have been varied in this study are for the polystyrene suspensions concentration, particle size, and thickness of the cell, and for the TiO_2 suspensions concentration and thickness of the cell. By using a special "difference technique" we have been able to observe low-order and high-order scattering pro-

cesses independently.[13,15]

This paper is organized as follows. In Sec. II we will review some scattering formalism, and treat our scalar isotropic theory. In Sec. III we will introduce a diffusion approach to these scattering equations, and compare this approach with the exact theory. In Sec. IV we will present our experimental data and interprete them as much as possible with the newly developed theory.

II. MULTIPLE-SCATTERING THEORY OF FINITE SLABS

A. Introduction

Systematic perturbation theory in terms of diagrammatic expansions is a fruitful way of describing wave propagation in random media. A very useful review has been published by Frisch.[30] One immediately distinguishes two cases as far as the character of the inhomogeneities is concerned. In continuous media it is not possible to pick out separate scattering particles whereas in media consisting of discrete scatterers individual scattering centers can be distinguished. The first case is more difficult as one needs all higher (static) spatial correlation functions to characterize the medium. In the continuous medium one usually relies on some simplifying assumption as (Gaussian) decoupling of higher-order processes. When dealing with single scattering units it is sometimes possible to find the scattering matrix S of the individual particles. Strictly speaking this is only possible when the particle is spherical (Mie scattering). (For a collection of papers dealing with single-particle scattering of arbitrary shape, see Ref. 31).

The system we will study is a collection of identical random scatterers in a slab. The direction perpendicular to the slab is the z direction and the slab is confined within $[0,d]$, so d is the thickness of the slab.

B. Amplitude Green's functions

In the one-particle case it is useful to separate the fluctuating part of the dielectric constant from the (empty) medium part as

$$n^2(\mathbf{r})=n^2[1+\mu(\mathbf{r})] , \tag{1}$$

in which case the wave equation can be written as

$$\Delta\Psi(\mathbf{r})+k_0^2\Psi(\mathbf{r})=-\mu(\mathbf{r})k_0^2\Psi(\mathbf{r}) , \tag{2}$$

where k_0 is the magnitude of the wave vector associated with the empty (that is without scatterers) medium, $k_0=2\pi/\lambda$. The empty-space Green's function for the amplitude is defined as the solution of

$$\Delta g(\mathbf{r}_1,\mathbf{r}_2)+k_0^2 g(\mathbf{r}_1,\mathbf{r}_2)=\delta(\mathbf{r}_1-\mathbf{r}_2) , \tag{3a}$$

which is given by

$$g(\mathbf{r}_1,\mathbf{r}_2)=-\frac{\exp(ik_0\,|\,\mathbf{r}_1-\mathbf{r}_2\,|\,)}{4\pi\,|\,\mathbf{r}_1-\mathbf{r}_2\,|} . \tag{3b}$$

Defining an incoming wave $\Psi_{\rm inc}(\mathbf{r}_1)$ as the solution of the wave equation without the presence of the scatterer, Eq. (2) can be transformed into

$$\Psi(\mathbf{r}_1)=\Psi_{\rm inc}(\mathbf{r}_1)-\int g(\mathbf{r}_1,\mathbf{r}_2)\mu(\mathbf{r}_2)k_0^2\Psi(\mathbf{r}_2)d\mathbf{r}_2 . \tag{4}$$

This equation can be solved formally by introducing the scattering operator $S(\mathbf{r}_1,\mathbf{r}_2)$:

$$\Psi(\mathbf{r}_1)=\Psi_{\rm inc}(\mathbf{r}_1)+\int g(\mathbf{r}_1,\mathbf{r}_2)S(\mathbf{r}_2,\mathbf{r}_3)\Psi_{\rm inc}(\mathbf{r}_3)d\mathbf{r}_2 d\mathbf{r}_3 . \tag{5}$$

Clearly the first-order solution is

$$S(\mathbf{r}_1,\mathbf{r}_2)=-\mu(\mathbf{r}_1)k_0^2\delta(\mathbf{r}_1-\mathbf{r}_2) . \tag{6}$$

Iteration of Eq. (4) results in an explicit sum of scattering events (we will not bother with the convergence of these series here). Each term in the series represents a higher-order scattering contribution (still for one particle). In Fig. 1 we have depicted this series for S in diagrams, where the conventions for drawing of diagrams of Fig. 2 have been used. To facilitate the treatment of many scatterers the particle has been labeled α. Defining the Fourier transform of $S(\mathbf{r}_1,\mathbf{r}_2)$ with respect to wave vectors $\mathbf{k}_{\rm in}$ and $\mathbf{k}_{\rm out}$ (incoming and outgoing wave vectors) results in the quantity $S(\mathbf{k}_{\rm out},\mathbf{k}_{\rm in})$, with $\mathbf{k}_{\rm in}$ on shell: $k_{\rm in}=k_0$; in general, the Fourier transform of a quantity $A(\mathbf{r}_1,\mathbf{r}_2)$ has as prefactor $(2\pi)^{-3}$ unless explicitly defined differently. The scattering amplitude $f(\mathbf{k}_{\rm out},\mathbf{k}_{\rm in})$ is introduced as

$$f(\mathbf{k}_{\rm out},\mathbf{k}_{\rm in})=-2\pi^2 S(\mathbf{k}_{\rm out},\mathbf{k}_{\rm in}) , \tag{7}$$

which by integrating over all scattering angles can be related to the scattering cross section

$$\sigma_{\rm sc}(k_{\rm in})=\int |f(\mathbf{k}_{\rm out},\mathbf{k}_{\rm in})|^2 d\Omega . \tag{8}$$

The optical theorem can be used to relate the cross section to the imaginary part of the S matrix for forward scattering.[30]

To discuss the many-particle problem we have to modify Eq. (1) into

$$n^2(\mathbf{r})=n^2\left[1+\sum_\alpha \mu(\mathbf{r}-\mathbf{r}_\alpha)\right] , \tag{9}$$

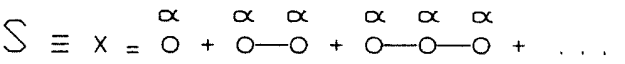

FIG. 1. Born series for the scattering operator.

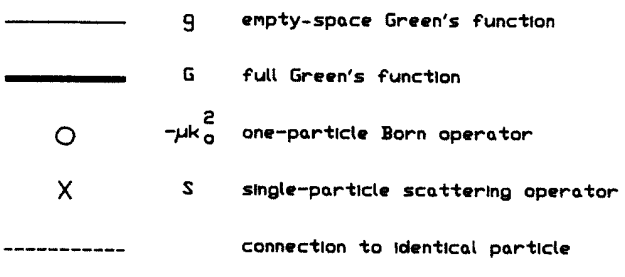

FIG. 2. Drawing convention for elements of diagrams.

where the summation is over the scattering centers. The full Green's function for the amplitude is defined as the solution of

$$\Delta G(\mathbf{r}_1,\mathbf{r}_2)+k_0^2 n^2(\mathbf{r}_1)G(\mathbf{r}_1,\mathbf{r}_2)=\delta(\mathbf{r}_1-\mathbf{r}_2) . \quad (10)$$

In many cases of Green's-function theory of random media statistical homogeneity is obtained by averaging over all the possible positions of the particles with, if necessary, taking into account particle-particle correlations. This gives rise to averaged Green's functions, which are defined by

$$\langle G(\mathbf{k}_1,\mathbf{k}_2)\rangle \equiv G(k)\delta(\mathbf{k}_1-\mathbf{k}_2) , \quad (11a)$$

or in real space

$$\langle G(\mathbf{r}_1,\mathbf{r}_2)\rangle \equiv G(\mathbf{r}_1-\mathbf{r}_2) . \quad (11b)$$

As averaged amplitude Green's functions depend only on one wave vector (or on one space coordinate) no confusion should arise with nonaveraged Green's functions. The difference between an empty-space Green's function and an averaged Green's function is that the former relates to the homogeneous medium without the presence of scattering units whereas in the latter a situation is described in which a configurational average has been performed with respect to the positions of all scattering particles. Only when matrix notation is used, explicit angular brackets will be employed to avoid confusion between averaged and nonaveraged quantities.

A useful equation can be obtained from Eq. (10) by introduction of the mass operator $\Sigma(\mathbf{r})$ defined by

$$G(\mathbf{r}_1)=g(\mathbf{r}_1)+\int g(\mathbf{r}_1-\mathbf{r}_2)\Sigma(\mathbf{r}_2-\mathbf{r}_3)G(\mathbf{r}_3)d\mathbf{r}_2 d\mathbf{r}_3 . \quad (12)$$

In order to allow for some formal manipulations and to get a more concise notation Eq. (12) can be put in matrix notation,

$$G=g+g\Sigma G , \quad (13)$$

which can be formally solved as

$$G=(g^{-1}-\Sigma)^{-1} . \quad (14)$$

In wave-vector space this inversion can be carried out immediately as

$$G(k)=g(k)+g(k)\Sigma(k)G(k) , \quad (15a)$$

which results in

$$G(k)=[g(k)^{-1}-\Sigma(k)]^{-1}=[k_0^2-k^2-\Sigma(k)]^{-1} . \quad (15b)$$

From (15b) it is clear that the average Green's function deviates from the empty-space Green's function by an effective wave vector $\mathbf{K}\equiv\mathbf{K}'+i\mathbf{K}''$, the magnitude of which is given by $K^2=k_0^2-\Sigma(k)$. The real part of K (K') describes a renormalized index of refraction and the imaginary part of K (K'') is connected with the (scattering) mean free path (inverse of the turbidity).

In Fig. 3 a diagrammatic expansion is given for the mass operator in case of absence of particle correlations.

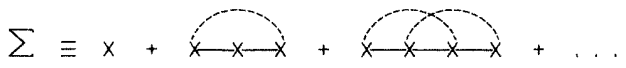

FIG. 3. Lowest-order contributions to the self-energy.

Successive scattering events cannot relate to the same particle, since they are already contained in the scattering operator $S(\mathbf{k}_1,\mathbf{k}_2)$. In the low-density approximation one finds [retaining only the first term of the expansion presented in Fig. (3)]

$$\Sigma(k)=(2\pi)^3 n_0 S(\mathbf{k},\mathbf{k}), \quad k=k_0 \quad (16)$$

in which n_0 is the density of scatterers. There are two reasons why this approximation will severely break down at high densities: (i) correlations of the scattering events (dependent scattering), and (ii) correlations of the scattering particles. The second effect is well known and corrections can be found for it (for instance, by using approaches originating from gas-kinetic theory such as the Percus-Yevick approach).[32] The complication of dependent scattering is very important with respect to the localization issue. Some attention has been paid to scattering effects of correlated particles.[32,33]

C. Intensity Green's functions

We now have to deal with Green's functions related to the intensity rather than to the amplitude. These functions are defined as the following tensor product:

$$H\equiv G\times G^* , \quad (17a)$$

i.e., the tensor product of the amplitude Green's function and its complex conjugate, in components

$$H(\mathbf{r}_1,\mathbf{r}_2,\mathbf{r}_3,\mathbf{r}_4)\equiv G(\mathbf{r}_1,\mathbf{r}_2)G^*(\mathbf{r}_3,\mathbf{r}_4) . \quad (17b)$$

Diagrammatic perturbation theory can easily be set up for this intensity Green's function as well.[30] We just double the diagrams and connect identical scattering centers by dashed lines (see Fig. 2). We will define the complete (reducible) vertex R as equal to the sum of all connected intensity diagrams H without the incoming and outgoing Green's function. The following matrix equation for $\langle H\rangle$ holds:

$$\langle H\rangle=\langle G\rangle\times\langle G^*\rangle + (\langle G\rangle\times\langle G^*\rangle)\langle R\rangle(\langle G\rangle\times\langle G^*\rangle) . \quad (18)$$

In Fig. 4 we have depicted some lower-order contributions to $\langle R\rangle$. The equivalent of the mass operator for

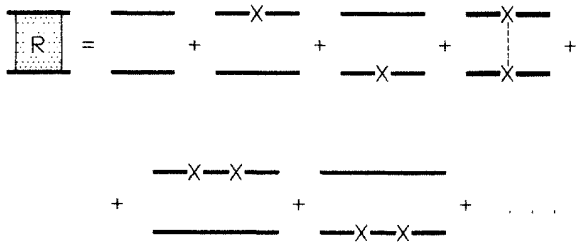

FIG. 4. Lowest-order contributions to the total vertex R.

this type of (intensity) Green's function is the irreducible vertex $\langle U \rangle$ defined for the averaged functions by

$$\langle H \rangle = \langle G \rangle \times \langle G^* \rangle + (\langle G \rangle \times \langle G^* \rangle)\langle U \rangle \langle H \rangle , \quad (19)$$

and $\langle U \rangle$ is generated by all double-connected diagrams. The relation between $\langle R \rangle$ and $\langle U \rangle$ is given by

$$\langle R \rangle = \langle U \rangle + (\langle G \rangle \times \langle G^* \rangle)\langle U \rangle \langle R \rangle . \quad (20)$$

In Fig. 5 some lower-order contributions to $\langle U \rangle$ are displayed. The incoherent contribution to these diagrams is given by retaining for $\langle U \rangle$ only the lowest-order term $\langle I \rangle$ which results in the summation of all ladder diagrams. This sum of all ladder diagrams (without ingoing and outgoing lines) will be called $\langle L \rangle$ (see Fig. 6). It turns out that the most important interference contribution arises from the interference from time-reversed paths (most-crossed diagrams). The sum of all most-crossed diagrams (without ingoing and outgoing lines) will be called $\langle C \rangle$ (see Fig. 7). For strong localization theory these most crossed diagrams have to be summed in the irreducible vertex $\langle U \rangle$, $\langle U \rangle = \langle I \rangle + \langle C \rangle$ (see Fig. 5).[34] However, in the weak regime, which is under study here, the most crossed diagrams can be summed in the Green's function itself, $\langle R \rangle = \langle L \rangle + \langle C \rangle$.[35] Localization as found in the diagrammatic theory comes about by finding a self-consistent equation which yields a vanishing of the diffusion coefficient in the strongly scattering regime.[3,7,8,34] Basically all these theories are based on ideas developed by Götze to describe localization of electrons.[36] Since in these theories one is only interested in transport coefficients, statistical homogeneity can be assumed. This amounts to a considerable simplification as use can be made of (statistical) translational symmetry.

Let us first discuss the incoherent contribution to the intensity Green's functions. To this end we have to sum the ladder contribution. The integral equation for $\langle L \rangle$ is

$$\langle L \rangle = \langle I \rangle + \langle I \rangle(\langle G \rangle \times \langle G^* \rangle)\langle L \rangle . \quad (21)$$

Next we introduce the assumption of point scatterers. That is to say

$$S_\alpha(\mathbf{r}_1,\mathbf{r}_2) = -4\pi f \delta(\mathbf{r}_1 - \mathbf{r}_\alpha)\delta(\mathbf{r}_2 - \mathbf{r}_\alpha) , \quad (22)$$

where α is a particle index. If we plug assumption (22) into the series expansion for $\langle L \rangle$ (see Fig. 6) we see that in each term the incoming space coordinates as well as the outgoing space coordinates have to be equal. So we will try the Ansatz of Tsang and Ishimaru[16]

$$\langle L(\mathbf{r}_1,\mathbf{r}_2;\mathbf{r}_3,\mathbf{r}_4)\rangle = n_0(4\pi)^2 f^2 \delta(\mathbf{r}_2 - \mathbf{r}_1)\delta(\mathbf{r}_3 - \mathbf{r}_1)\delta(\mathbf{r}_4 - \mathbf{r}_1) + F(\mathbf{r}_1,\mathbf{r}_2)\delta(\mathbf{r}_1 - \mathbf{r}_3)\delta(\mathbf{r}_2 - \mathbf{r}_4) , \quad (23)$$

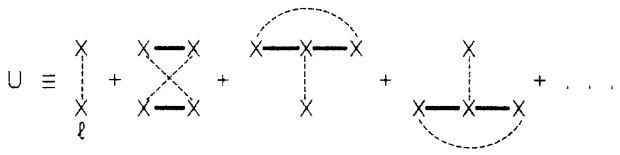

FIG. 5. Lowest-order contributions to the irreducible vertex U.

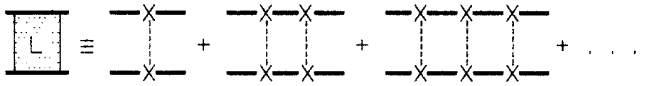

FIG. 6. Summation of ladder terms.

where the first-order term has explicitly been separated out. Insertion of this Ansatz into Eq. (21) yields an integral equation for $F \equiv F(\mathbf{r}_1,\mathbf{r}_2)$ which in matrix form is given by

$$F = n_0^2(4\pi f)^4 \langle G \rangle^2 + n_0(4\pi f)^2 \langle G \rangle^2 F . \quad (24)$$

This equation allows for an interpretation of F. Apparently F is the Green's function for the incoherent intensity or incoherent energy density. $F(\mathbf{r}_1,\mathbf{r}_2)$ describes the energy density at $\mathbf{r}_1$ due to a point source at $\mathbf{r}_2$. If a different source is being used (like a damped plane wave) the incoherent energy density can be obtained by integrating the Green's function F over this new source.

In the same way as we did for the ladder diagrams one can solve the summation of most crossed diagrams.[37] The best way is to disentangle the crossed diagrams. To this end we have put arrows on the diagrams for $\langle C \rangle$ to indicate the sense. Let us now look at a typical diagram and rotate the lower part 180°. It now looks very much like a ladder diagram. So if we would include the (nondegenerate) first-order scattering, the summation of crossed diagrams is exactly equal to the ladder sum (for point scatterers) if we permute the appropriate coordinates. So the sum of all most-crossed diagrams is also determined by F:

$$\langle C(\mathbf{r}_1,\mathbf{r}_2;\mathbf{r}_3,\mathbf{r}_4)\rangle = F(\mathbf{r}_1,\mathbf{r}_2)\delta(\mathbf{r}_2 - \mathbf{r}_3)\delta(\mathbf{r}_1 - \mathbf{r}_4) . \quad (25)$$

Apparently this tremendous simplification was missed in Ref. 16 (see also Ref. 5). A major part of our task has been fulfilled now. We have found an integral equation, the solution of which can be used to obtain the incoherent and time-reversed interference contributions, as described by the ladder- and most-crossed diagrams, to the intensity.

The F propagator obeys Eq. (24) which in components is given by

$$F(\mathbf{r}_1,\mathbf{r}_2) = n_0^2(4\pi)^2 |f|^4 A(\mathbf{r}_1 - \mathbf{r}_2) + n_0 |f|^2 \int A(\mathbf{r}_1 - \mathbf{r}')F(\mathbf{r}',\mathbf{r}_2)d\mathbf{r}' , \quad (26a)$$

with

$$A(\mathbf{r}_1,\mathbf{r}_2) = A(\mathbf{r}_1 - \mathbf{r}_2) = (4\pi)^2 \langle G \rangle^2 \frac{\exp(-\kappa |\mathbf{r}_1 - \mathbf{r}_2|)}{|\mathbf{r}_1 - \mathbf{r}_2|^2} , \quad (26b)$$

where $\kappa \equiv 2K'' \equiv \lambda_{MF}^{-1}$ is the extinction rate or turbidity,

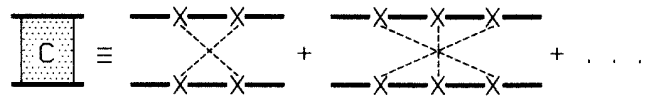

FIG. 7. Summation of most-crossed diagrams.

with λ_{MF} the mean free path. Notice that all the spatial integrations for F and related functions are integrations within the slab and not over full space. Using the translational invariance in the (x,y) plane we define the two-dimensional Fourier transform to be

$$F(\mathbf{r}_1,\mathbf{r}_2)=F(\mathbf{r}_\perp,z_1,z_2)$$
$$=(2\pi)^{-2}\int F(\mathbf{q}_\perp,z_1,z_2)\exp(i\mathbf{r}_\perp\cdot\mathbf{q}_\perp)d\mathbf{q}_\perp\ , \tag{27}$$

where $\mathbf{r}_\perp=(x_1-x_2,y_1-y_2)$. Consequently we have, with $a\equiv 4\pi n_0|f|^2/\kappa$ the (dimensionless) albedo, and with d the thickness of the slab

$$F(\mathbf{r}_\perp,z_1,z_2)=(\kappa a)^2 A(|\mathbf{r}_\perp|,|z_1-z_2|)$$
$$+\frac{\kappa a}{4\pi}\int\int A(|\mathbf{r}_\perp-\mathbf{r}'_\perp|,|z_1-z'|)$$
$$\times F(\mathbf{r}'_\perp,z',z_2)d\mathbf{r}'_\perp dz'\ , \tag{28a}$$

which gives after Fourier transformation

$$F(\mathbf{q}_\perp,z_1,z_2)=(\kappa a)^2 A(\mathbf{q}_\perp,|z_1-z_2|)$$
$$+\pi\kappa a\int A(\mathbf{q}_\perp,|z_1-z'|)$$
$$\times F(\mathbf{q}_\perp,z',z_2)dz'\ , \tag{28b}$$

and

$$A(\mathbf{q}_\perp,z)=\int A(\mathbf{r}_\perp,z)\exp(-i\mathbf{r}_\perp\cdot\mathbf{q}_\perp)d\mathbf{r}_\perp=\int\int\frac{\exp[-\kappa(r_\perp^2+z^2)^{1/2}]}{r_\perp^2+z^2}\exp(-ir_\perp q_\perp\cos\varphi)r_\perp dr_\perp d\varphi$$
$$=2\pi\int r_\perp J_0(r_\perp q_\perp)\frac{\exp[-\kappa(r_\perp^2+z^2)^{1/2}]}{r_\perp^2+z^2}dr_\perp$$
$$=2\pi\int_1^\infty\frac{\exp[-\kappa z(t^2+\alpha^2)^{1/2}]}{(t^2+\alpha^2)^{1/2}}dt\equiv 2\pi W(\tau,\alpha)\ , \tag{28c}$$

where $J_0(x)$ is the Bessel function of zeroth order and argument x (see Ref. 38), and in which $\tau\equiv\kappa z$, and

$$\alpha\equiv\frac{q_\perp}{\kappa}=\frac{k_0}{\kappa}[(\sin\theta_i\cos\varphi_i+\sin\theta_s\cos\varphi_s)^2$$
$$+(\sin\theta_i\sin\varphi_i+\sin\theta_s\sin\varphi_s)^2]^{1/2}\ , \tag{28d}$$

where the polar angles refer to the incoming $\hat{\mathbf{K}}_i$ and to the scattered direction $\hat{\mathbf{K}}_s$. Notice that $W(\tau,\alpha=0)=E_1(\tau)$, the exponential integral. For reasons of convention we define

$$\Gamma(\tau_1,\tau_2;\alpha)\equiv\frac{1}{4\pi\kappa^2}F(\mathbf{q}_\perp,z_1,z_2)\ , \tag{29}$$

and the (dimensionless) optical thickness $b\equiv\kappa d$ so

$$\Gamma(\tau_1,\tau_2;\alpha)=\frac{a^2}{2}W(|\tau_1-\tau_2|;\alpha)$$
$$+\frac{a}{2}\int_0^b W(|\tau_1-\tau'|;\alpha)\Gamma(\tau',\tau_2;\alpha)d\tau'\ . \tag{30}$$

Equation (30) has the form of the Milne equation. It is a Fredholm integral equation of the second kind with singular kernel.[39] Notice the extremely useful property that $\Gamma(\tau_1,\tau_2;\alpha)$ is only coupled to elements of Γ with the same value of τ_2. So apart from the connection through the initial source term the τ_1 dependence of Γ is decoupled from the τ_2 dependence.

To allow for easy formal manipulations it is very useful to introduce the following matrix multiplication. For matrices $\mathcal{F}$ and $\mathcal{G}$ it is defined as

$$\mathcal{F}\mathcal{G}=\int_0^b\mathcal{F}(\tau)\mathcal{G}(\tau)d\tau\ . \tag{31}$$

Notice that if the matrices depend on two τ coordinates the multiplication only involves the first coordinate. With

$$M(\tau_1,\tau_2;\alpha)\equiv\tfrac{1}{2}W(|\tau_1-\tau_2|;\alpha)\ , \tag{32}$$

Equation (30) can be written in matrix form

$$\Gamma=S+aM\Gamma\ , \tag{33}$$

where the initial source, $S=a^2M$, represents two-particle scattering. Taking as initial source $S=a\delta(\tau_1-\tau_2)$ would include single scattering in Γ. Notice that both of these terms are unbound for $\tau_1\to\tau_2$. The formal solution of Eq. (33) is

$$\Gamma=(\mathbb{1}-aM)^{-1}S\ , \tag{34}$$

so the solution of the total scattering problem can be obtained by inverting the matrix $(\mathbb{1}-aM)$. It may also be developed into a power series, in which case the solution takes the form

$$\Gamma=S+aMS+a^2M^2S+a^3M^3S+\cdots\ , \tag{35}$$

in which each term is found by multiplying the preceding

one with the matrix aM. The physical significance of the power series is that each term corresponds to a separate order of scattering.

Equation (30) is in such a form that direct numerical determination of Γ becomes feasible. The numerical procedure will be dealed with in Sec. II E and in Appendixes A–C.

D. Scattering intensity

We have to emphasize that to describe a real *scattering* experiment one cannot assume that the system exhibits statistical translational symmetry. The practical solution to this complication is to perform the calculation in the real-space domain and limit the integration over space in such a way that only the integration over the finite sample is performed. Properly speaking this is only feasible when one assumes a S matrix which is so extremely simple that the integrations in real space can actually be performed, viz., point scatterers.

To describe a scattering experiment we have to consider an inhomogeneous medium since in such an experiment separation of source, target, and detector are required. To arrive at the result for the scattered intensity we consider the Green's function for the intensity $\langle \Psi \times \Psi^* \rangle$, which using Eq. (12) is given by

$$\langle \Psi \times \Psi^* \rangle = \langle \Psi_{\rm inc} \rangle \times \langle \Psi^*_{\rm inc} \rangle + (\langle G \rangle \times \langle G^* \rangle)\langle R \rangle (\langle \Psi_{\rm inc} \rangle \times \langle \Psi^*_{\rm inc} \rangle) . \tag{36}$$

For the intensity we need $I(\mathbf{r}) \equiv \Psi(\mathbf{r})\Psi^*(\mathbf{r})$ which can be found by writing Eq. (36) in its components

$$\begin{aligned} \langle I(\mathbf{r}_1) \rangle &\equiv \langle \Psi(\mathbf{r}_1)\Psi^*(\mathbf{r}_1) \rangle \\ &= \langle \Psi_{\rm inc}(\mathbf{r}_1) \rangle \langle \Psi^*_{\rm inc}(\mathbf{r}_1) \rangle \\ &\quad + \int \langle G(\mathbf{r}_1 - \mathbf{r}_2) \rangle \langle G^*(\mathbf{r}_1 - \mathbf{r}_3) \rangle \langle R(\mathbf{r}_2, \mathbf{r}_3; \mathbf{r}_4, \mathbf{r}_5) \rangle \langle \Psi_{\rm inc}(\mathbf{r}_4) \rangle \langle \Psi^*_{\rm inc}(\mathbf{r}_5) \rangle d\mathbf{r}_2 d\mathbf{r}_3 d\mathbf{r}_4 d\mathbf{r}_5 . \end{aligned} \tag{37}$$

The mean-field amplitude and Green's function depend on the propagation constant in the medium which for point scatterers can be calculated to be

$$K \equiv K' + iK'' , \tag{38a}$$

$$K = k_0 + \frac{2\pi n_0 f}{k_0} . \tag{38b}$$

The mean-field amplitude function is

$$\langle \Psi_{\rm inc}(\mathbf{r}_1) \rangle = \exp(i\mathbf{K}_i \cdot \mathbf{r}_1) , \tag{39a}$$

where $\mathbf{K}_i$ is a vector with magnitude K and direction of the incoming wave in the medium. For almost normal incidence $\mathbf{K}_i$ can be approximated by

$$\mathbf{K}_i = \hat{\mathbf{x}} k_0 \sin\theta_i \cos\varphi_i + \hat{\mathbf{y}} k_0 \sin\theta_i \sin\varphi_i - \hat{\mathbf{z}} K_{iz} , \tag{39b}$$

$$K_{iz} = k_0 \cos\theta_i - \frac{iK''}{\cos\theta_i} . \tag{39c}$$

The mean Green's function is given by

$$\langle G(\mathbf{r}_1 - \mathbf{r}_2) \rangle = -\frac{\exp(iK \mid \mathbf{r}_1 - \mathbf{r}_2 \mid)}{4\pi \mid \mathbf{r}_1 - \mathbf{r}_2 \mid} , \tag{40a}$$

when $\mathbf{r}_1$ and $\mathbf{r}_2$ are inside the slab, and

$$\langle G(\mathbf{r}_1, \mathbf{r}_2) \rangle \simeq -\frac{e^{ik_0 r_1}}{4\pi r_1} \exp(-i\mathbf{K}_s \cdot \mathbf{r}_2) , \tag{40b}$$

when $\mathbf{r}_2$ is in the slab, and when $\mathbf{r}_1$ is far outside the slab, and where the outgoing wave vector $\mathbf{K}_s$ is given approximately by

$$\mathbf{K}_s = \hat{\mathbf{x}} k_0 \sin\theta_s \cos\varphi_s + \hat{\mathbf{y}} k_0 \sin\theta_s \sin\varphi_s - \hat{\mathbf{z}} K_{sz} , \tag{40c}$$

$$K_{sz} = k_0 \cos\theta_s - \frac{iK''}{\cos\theta_s} . \tag{40d}$$

The scattering intensity is best described with the help of the so-called bistatic scattering coefficient.[26] The partitioning of the total bistatic scattering coefficient into the coefficients for single scattering, ladder, and cyclical intensities, is given by

$$\begin{aligned} \gamma(\mu_s, \mu_i) &\equiv \frac{4\pi r^2}{A\mu_i} I(\mathbf{r}) \\ &= \gamma_s(\mu_s, \mu_i) + \gamma_l(\mu_s, \mu_i) + \gamma_c(\mu_s, \mu_i) , \end{aligned} \tag{41a}$$

where A is the area of the target, and $\mu_{i,s} \equiv \cos\theta_{i,s}$. Calculating $\langle R \rangle = \langle L \rangle + \langle C \rangle$, in which $\langle L \rangle$ is given by (23) and $\langle C \rangle$ given by (25), and employing also Eqs. (39a), (40b), and definition (29) in Eq. (37) gives

$$\gamma_s(\mu_s, \mu_i) = \frac{a\mu_s}{\mu_i + \mu_s} \left\{ 1 - \exp\left[-b \left(\frac{1}{\mu_i} + \frac{1}{\mu_s} \right) \right] \right\} , \tag{41b}$$

$$\gamma_l(\mu_s, \mu_i) = \frac{1}{\mu_i} \int_0^b \int_0^b \Gamma(\tau_1, \tau_2; \alpha = 0) \exp\left[-\left(\frac{\tau_1}{\mu_s} + \frac{\tau_2}{\mu_i} \right) \right] d\tau_1 d\tau_2 , \tag{41c}$$

$$\gamma_c(\mu_s, \mu_i) = \frac{1}{\mu_i} \int_0^b \int_0^b \Gamma(\tau_1, \tau_2; \alpha) \cos\left[\frac{k_0}{\kappa} (\mu_i - \mu_s)(\tau_1 - \tau_2) \right] \exp\left[-\frac{1}{2} \left(\frac{1}{\mu_s} + \frac{1}{\mu_i} \right) (\tau_1 + \tau_2) \right] d\tau_1 d\tau_2 , \tag{41d}$$

in agreement with Ref. 16.

We have indicated that the Green's function Γ can be used to calculate the energy density in the slab [see remark following Eq. (24)]. In the present case the incoming (reduced) intensity I_{ri} is given by

$$I_{ri}(\tau,\hat{\mathbf{k}})=\exp(-\tau/\mu_i)\delta(\hat{\mathbf{k}}-\hat{\mathbf{K}}_i)\ , \tag{42}$$

where $\hat{\mathbf{K}}_i$ is the incoming direction. The energy density or the so-called source function $J(\tau)$ which is extensively studied in the literature,[26,27] is given by

$$J(\tau)=\int_0^b \Gamma(\tau,\tau';\alpha=0)\exp(-\tau'/\mu_i)d\tau'\ , \tag{43}$$

and using the (complicated) integral equation for Γ as given by Eq. (30) one derives a much simpler equation for the incoherent energy density

$$J(\tau)=\frac{a^2}{2}\int_0^b E_1(|\tau-\tau'|)\exp(-\tau'/\mu_i)d\tau' + \frac{a}{2}\int_0^b E_1(|\tau-\tau'|)J(\tau')d\tau'\ , \tag{44}$$

which is the Schwarzschild-Milne equation with the source term describing second-order scattering. The incoherent contribution to the bistatic coefficient can also be expressed in terms of the energy density,

$$\gamma_I(\mu_s,\mu_i)=\frac{1}{\mu_i}\int_0^b J(\tau)\exp(-\tau/\mu_s)d\tau\ . \tag{45}$$

So if one is only interested in the ladder contribution to the scattering, the determination of the Green's function $\Gamma(\tau_1,\tau_2)$ is not necessary as the determination of energy density $J(\tau)$ is sufficient. This is a substantial simplification. The (numerical) determination of the solution of the Schwarzschild-Milne equation is straightforward.[16,26,27,40]

E. Numerical results of Γ and the line shape γ

The general outline is quite straightforward. We have to solve the integral equation (30) numerically and then use the result to calculate the bistatic scattering coefficient $\gamma(\mu_s,\mu_i)$. To do this, we have to calculate the kernel $W(\tau,\alpha)$ first. This problem is discussed in Appendix A.

To calculate the scattering problem, it is also important to notice the following symmetry properties of Γ:

$$\Gamma(\tau_1,\tau_2)=\Gamma(\tau_2,\tau_1)=\Gamma(b-\tau_1,b-\tau_2)\ . \tag{46}$$

Γ may be written as a sum of the contributions of the separate orders of scattering. So the total solution is given by

$$\Gamma=\lim_{N\to\infty}\sum_{n=2}^{N}\Gamma_n\ , \tag{47}$$

in which $\Gamma_n(\tau_1,\tau_2;\alpha)$ represents the contribution for the nth order of scattering. We can use the iterative formula

$$\Gamma_{n+1}(\tau_1,\tau_2;\alpha)=\frac{a}{2}\int_0^b W(|\tau_1-\tau'|;\alpha)\Gamma_n(\tau',\tau_2;\alpha)d\tau'\ , \tag{48a}$$

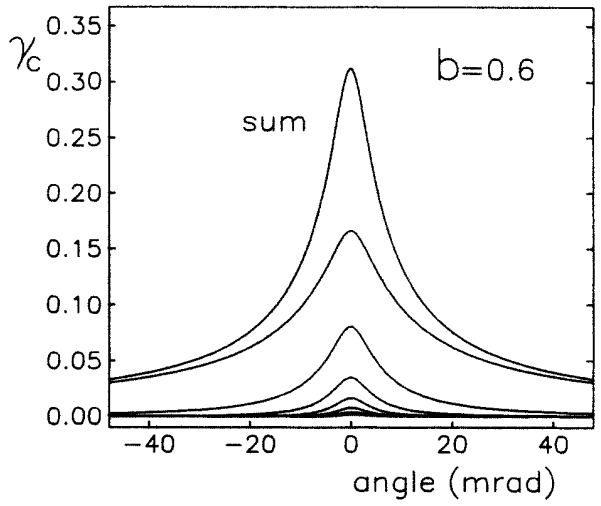

FIG. 8. Line shape of the enhanced backscattering of the second up to the eighth order of scattering and their sum for slab thickness $b=0.6$, $\lambda_{MF}/\lambda=53.5$, and albedo $a=1$.

or

$$\Gamma_{n+1}=aM\Gamma_n\ , \tag{48b}$$

to calculate the successive orders of scattering, starting with

$$S=a^2M=\frac{a^2}{2}W(|\tau_1-\tau_2|;\alpha)\equiv\Gamma_2\ . \tag{49}$$

The details of this calculation are presented in Appendix B.

The convergence of our iterative procedure to the total solution Γ is, except for numerical problems that might occur due to build up of inaccuracy for very high orders of scattering, determined by the albedo a and the optical thickness of the slab b. The thicker the slab and the closer the albedo to 1, the slower the convergence. So albedo close to one is the most difficult and albedo substantially less than one becomes almost trivial. For a semi-infinite slab, the iteration converges as $a^n n^{-3/2}$. In practice this means that it is possible to calculate the whole solution for $b=\infty$ and $a<0.9$ within 1% accuracy in less than 20 iterations. For the albedo $a=1$ only slabs with $b<2$ can be treated with about the same accuracy. In Fig. 8 the order by order line shape is given for a typical case.

Of course we are also interested in thick slabs ($b>2$) with the albedo close or equal to 1. The solution to this problem is obtained by solving Eq. (30) by diagonalization (see Appendix C). With the diagonalization procedure we can handle slabs up to 32 optical depths with albedo equal to 1. In Sec. IV we will compare the results from the theory with various experiments. If more sophisticated discretization procedures would be invoked we probably could extend this limit substantially. Yet, the backscattering intensity from the $b=32$ slab is already 95% of the backscattering of the semi-infinite slab. So the only problem left, are very thick slabs ($32<b<\infty$) in case $a=1$. However, thick slabs and

dominance of high-order scattering processes are precisely the conditions for which a diffusion approximation should hold.

III. DIFFUSION APPROXIMATION FOR FINITE SLABS

First we consider a scattering medium of infinite size and take advantage of the translational invariance in all directions. The three-dimensional Fourier transform is

$$\begin{aligned} F(\mathbf{r}_1,\mathbf{r}_2) &\equiv F_0(\mathbf{r}_1-\mathbf{r}_2) \\ &\equiv F_0(\mathbf{r}) \\ &\equiv (2\pi)^{-3}\int F_0(\mathbf{q})\exp(i\mathbf{r}\cdot\mathbf{q})d\mathbf{q} \ . \end{aligned} \tag{50}$$

With Eq. (26) we find

$$F_0(\mathbf{q}) = 2\pi^2 a\kappa A(\mathbf{q})F(\mathbf{q}) + a^2\kappa^2 A(\mathbf{q}) \ , \tag{51}$$

so that

$$F_0(\mathbf{r}) = a^2\kappa^2(2\pi)^{-3}\int \frac{A(\mathbf{q})}{1+2\pi^2 a\kappa A(\mathbf{q})}\exp(i\mathbf{r}\cdot\mathbf{q})d\mathbf{q} \ , \tag{52}$$

$A(\mathbf{q})$ can be calculated as

$$\begin{aligned} A(\mathbf{q}) &\equiv \int A(\mathbf{r})\exp(-i\mathbf{r}\cdot\mathbf{q})d\mathbf{r} \\ &= \int\int\int \exp(-\kappa r)\exp(-irq\cos\theta)\sin\theta\, d\varphi\, d\theta\, dr \\ &= (4\pi/q)\int_0^\infty \frac{1}{r}\exp(-\kappa r)\sin(qr)dr \\ &= (4\pi/q)\arctan(q/\kappa) \ , \end{aligned} \tag{53}$$

substituting this result in (52) and performing the angular integration gives

$$F_0(r) = \frac{2a^2\kappa^2}{\pi r}\int_0^\infty \frac{(q/\kappa)\arctan(q/\kappa)}{(q/\kappa)-(a)\arctan(q/\kappa)} \times \sin(qr)dq \ . \tag{54}$$

The solutions for all definite integrals used in this section can be found in Refs. 38 and 41.

For the diffusive regime we have $q \ll \kappa$ and we can approximate arctan (q/κ) by

$$\arctan(x) \simeq \frac{x}{1+\frac{1}{3}x^2}, \quad |x|<1 \ . \tag{55}$$

Notice that this approximation provides a useful cutoff for $q>\kappa$. So with $\kappa_a^2 \equiv 3\kappa^2(1-a)$ we find

$$\begin{aligned} F_0(r) &= \frac{2a^2\kappa^2}{\pi r}\int_0^\infty \frac{3q}{q^2+\kappa_a^2}\sin(qr)dq \\ &= \frac{3a^2\kappa^3}{r}\exp(-\kappa_a r) \ , \end{aligned} \tag{56}$$

which can only be justified for albedo a close to 1. So the solution of (26) in the diffusion approximation for an infinite space is given by

$$\begin{aligned} F(\mathbf{r}_1,\mathbf{r}_2) &= F_0(\mathbf{r}_1-\mathbf{r}_2) \\ &= F_0(\mathbf{r}_\perp,z) \\ &= \frac{3a^2\kappa^3}{|\mathbf{r}_1-\mathbf{r}_2|}\exp(-\kappa_a|\mathbf{r}_1-\mathbf{r}_2|) \ . \end{aligned} \tag{57}$$

Define

$$F_0(\mathbf{q}_\perp,z) \equiv \int F_0(\mathbf{r}_\perp,z)\exp(-i\mathbf{r}_\perp\cdot\mathbf{q}_\perp)d\mathbf{r}_\perp \ . \tag{58a}$$

This gives

$$F_0(\mathbf{q}_\perp,z) = 2\pi\int r_\perp J_0(r_\perp q_\perp) \times \frac{\exp[-\kappa_a(r_\perp^2+z^2)^{1/2}]}{(r_\perp^2+z^2)^{1/2}}dr_\perp \ , \tag{58b}$$

so that

$$\begin{aligned} F_0(\mathbf{q}_\perp,z) &= 6\pi a^2\kappa^3(\kappa_a^2+q_\perp^2)^{-1/2} \\ &\quad \times \exp[-z(\kappa_a^2+q_\perp^2)^{-1/2}] \ . \end{aligned} \tag{58c}$$

Up to now we have considered the statistical homogeneous (infinite) system. One has to include boundary conditions to handle the finite slab problem. From the literature[26,27,29,42] we know that the boundary conditions are $F(x_1-x_2,y_1-y_2,-z_0)=0$ and $F(x_1-x_2,y_1-y_2,d+z_0)=0$, which corresponds to a trapping plane in $-z_0$ and $d+z_0$, respectively. It appears that $z_0 \simeq 0.7104\lambda_{\mathrm{MF}}$ for $a=1$. A diffusion equation with trapping planes can be handled in a straightforward way.[43] The solution of (26) for a finite slab in the diffusion approximation is

$$\begin{aligned} F(\mathbf{r}_1,\mathbf{r}_2) = \sum_{n=-\infty}^{\infty} & F_0[x_1-x_2,y_1-y_2,z_1-z_2+2n(d+2z_0)] \\ & -F_0[x_1-x_2,y_1-y_2,z_1+z_2 \\ & +2n(d+2z_0)+2z_0] \ . \end{aligned} \tag{59}$$

The summation in this equation results from the multiple reflection of F in both mirror planes. It is obvious that the thicker the slab, the lower the number of contributing terms. For a semi-infinite slab, only the term for $n=0$ remains. From definition (29) and Eqs. (58c) and (59) it follows:

$$\begin{aligned} \Gamma(\tau_1,\tau_2;\alpha) &= \frac{3a^2}{2c}\sum_{n=-\infty}^{\infty}[\exp(-c|\tau_1-\tau_2+2nB|) \\ &\quad -\exp(-c|\tau_1+\tau_2+2nB+2\tau_0|)] \ , \end{aligned} \tag{60a}$$

with

$$c \equiv [3(1-a)+\alpha^2]^{1/2} , \tag{60b}$$

$$\tau_0 \equiv \kappa z_0 , \tag{60c}$$

$$B \equiv b + 2\tau_0 . \tag{60d}$$

Let us define

$$\Gamma'(\delta,\sigma;\alpha) \equiv \Gamma(\tau_1,\tau_2;\alpha) , \tag{61a}$$

$$\delta \equiv \tau_1 - \tau_2 , \tag{61b}$$

$$\sigma \equiv \tau_1 + \tau_2 . \tag{61c}$$

After some algebra it turns out that the summation can actually be performed and we get the Green's function Γ in closed form

$$\Gamma'(\delta,\sigma;\alpha) = \frac{3a^2}{2c\sinh(cB)} \{\cosh[c(B-|\delta|)] - \cosh[c(b-\sigma)]\} . \tag{62}$$

This result can be used to calculate the incoherent energy density or source function $J(\tau)$. From Eqs. (43), (61), and (62) it follows that for a semi-infinite slab ($b = \infty$) the result is given by

$$J_\infty(\tau) = \frac{3a^2\mu_i}{1-\mu_i^2c^2}[2Q_+ \exp(-c\tau) - \mu_i \exp(-\tau/\mu_i)] , \tag{63a}$$

with

$$Q_\pm \equiv [1+\mu_i c - (1\mp\mu_i c)\exp(-2c\tau_0)]/4c . \tag{63b}$$

The bistatic coefficient arising from the incoherent scattering in the diffusion approximation for the semi-infinite slab is calculated to be

$$\gamma_{I,\infty} = \frac{3a^2\mu_s}{1-\mu_i^2c^2}[2Q_+/(1+\mu_s c) - \mu_i^2/(\mu_i+\mu_s)] . \tag{64}$$

For a finite slab the results are considerably more complicated:

$$J(\tau) = \frac{3a^2\mu_i}{1-\mu_i^2c^2}\{P_+ \exp(-c\tau) - P_- \exp[c(\tau+2\tau_0)] - \mu_i \exp(-\tau/\mu_i)\} , \tag{65}$$

and

$$\gamma_I = \frac{3a^2\mu_s}{1-\mu_i^2c^2}\left[\frac{\mu_i^2}{\mu_i+\mu_s}\left\{\exp\left[-b\left[\frac{1}{\mu_i}+\frac{1}{\mu_s}\right]\right]-1\right\} + \frac{P_+}{1+\mu_s c}\left\{1-\exp\left[-b\left[c+\frac{1}{\mu_s}\right]\right]\right\} + \frac{P_-}{1-\mu_s c}\exp(2c\tau_0)\left\{\exp\left[b\left[c-\frac{1}{\mu_s}\right]\right]-1\right\}\right] . \tag{66}$$

Of course when discussing weak localization of light, one is more interested in the interference contributions than in the incoherent part. However, it is very important to consider the incoherent part as well. The reason is that Eqs. (64) and (66) are a consequence of the diffusion approximation which can be checked against *rigorous* answers. The Milne equation (44) can be solved exactly for all slab thicknesses by numerical methods. The exact results should be compared with the results obtained in Eqs. (64) and (66). This constitutes a stringent test on the validity of the diffusion theory. It turns out that the results are very good indeed, as will be shown later.

Let us now consider the interference contribution to the scattering in the diffusion approximation. We define

$$u \equiv \frac{k_0}{\kappa}(\mu_i - \mu_s) , \tag{67a}$$

$$v \equiv \frac{1}{2}\left[\frac{1}{\mu_i}+\frac{1}{\mu_s}\right] . \tag{67b}$$

Using Eq. (41d), definition (61a), and the diffusion result Eq. (62) the bistatic scattering coefficient for the interference (most-crossed diagrams) terms can easily be shown to be

$$\gamma_c(\mu_s,\mu_i) = \frac{1}{\mu_i}\int_0^b \int_\delta^{2b-\delta} \Gamma'(\delta,\sigma;\alpha)\cos(u\delta) \times \exp(-v\sigma)\, d\sigma\, d\delta . \tag{68a}$$

After tedious algebra we find

$$\gamma_c(\mu_s,\mu_i)=\frac{3a^2\exp(-vb)}{2\mu_i cv\sinh(cB)}\left[\left[\frac{1}{(v-c)^2+u^2}[v-(v-c)\cosh(2c\tau_0)]\right.\right.$$
$$\left.+\frac{1}{(v+c)^2+u^2}[v-(v+c)\cosh(2c\tau_0)]\right]\cos(ub)$$
$$+\left[\frac{u}{(v+c)^2+u^2}-\frac{u}{(v-c)^2+u^2}\right]\sinh(2c\tau_0)\sin(ub)$$
$$+\frac{1}{(v-c)^2+u^2}\{(v-c)\cosh[(v-c)b-2c\tau_0]-(v)\cosh[(v-c)b]\}$$
$$\left.+\frac{1}{(v+c)^2+u^2}\{(v+c)\cosh[(v+c)b+2c\tau_0]-(v)\cosh[(v+c)b]\}\right]. \quad (68b)$$

Note that for pure backscattering, $\mu_i=\mu_s$, $\gamma_l=\gamma_c$ in all cases. For $b\to\infty$ expression (68b) reduces to

$$\gamma_{c,\infty}=\frac{3a^2\{c+v[1-\exp(-2c\tau_0)]\}}{2\mu_i cv[(v+c)^2+u^2]}. \quad (69)$$

For an albedo of 1 this agrees with the result of Ref. 17. In Figs. 9–13 we present the bistatic scattering coefficient γ and the width of the backscattering cone as a function of the optical thickness b and the mean free path λ_{MF}. For a number of cases the results are compared with the exact values calculated with the rigorous theory from Sec. II.

There are no reasons to expect the diffusion approximation to be correct for low values of the albedo a. However, if we compare the behavior of this theory with the exact theory (see Fig. 9 for comparison of the intensities for precisely backscattering), we conclude that the agreement between the two theories is quite good, even for small albedos.

In Fig. 10 we compare the line shapes of the exact theory and the diffusion approximation for two different optical thicknesses, with the albedo $a=1$. We see that although their shapes are comparable, the diffusion approximation shows a small underestimation for all angles with respect to the exact theory. Later (Fig. 14 and Table I) we will see that this is caused by a small underestimation of the lowest orders of scattering. This also explains why the line shapes for thin slabs (which consequently contain a lot of low-order scattering) suffer more from this underestimation than those for thick slabs.

In Fig. 11 we present the (full width at half maximum) linewidth W as a function of the mean free path. From this we conclude that $W(\lambda_{MF}/\lambda)$ is a constant for a fixed albedo and slab thickness $b=\infty$, at least for $(\lambda_{MF}/\lambda)>1$. After a detailed study, we have found this to be true for any other value of b as well, as long as the latter condition is fulfilled. This conclusion is used in Fig. 12 to plot the value $W(\lambda_{MF}/\lambda)$ against the optical thickness b. The discrepancy between the exact theory and the diffusion

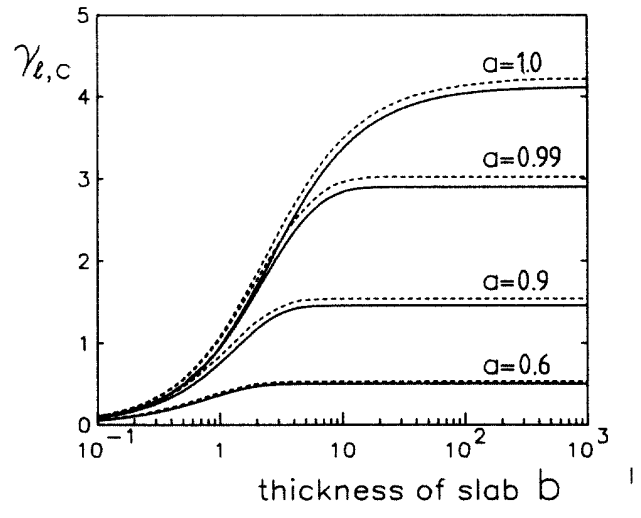

FIG. 9. Absolute values of $\gamma_{l,c}$ at exactly backscattering $[\gamma_l(\mu_s=\mu_i,\mu_i)=\gamma_c(\mu_s=\mu_i,\mu_i)]$ with $\mu_i=1$, as a function of the optical thickness b. Dashed curves represent the result from the exact theory as derived in Sec. II, solid lines give the result from the diffusion approximation. Different curves correspond to different albedos.

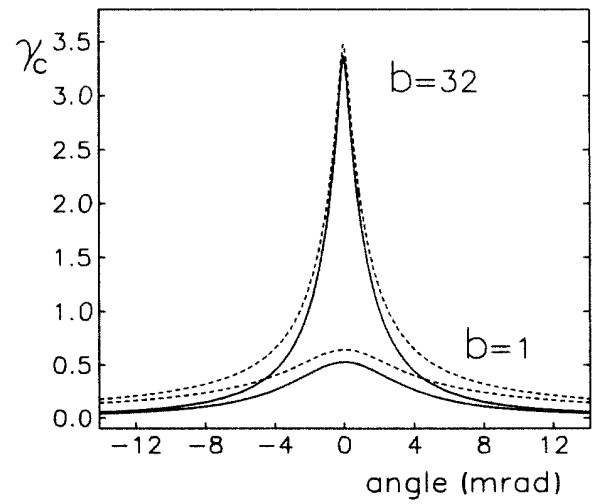

FIG. 10. Comparison of the absolute line shapes $\gamma_c(\mu_s,\mu_i=1)$ as found from the exact theory (dashed lines) and the diffusion approximation (solid lines) for slab thickness $b=32$ and $b=1$, $\lambda_{MF}/\lambda=53.5$, and albedo $a=1$.

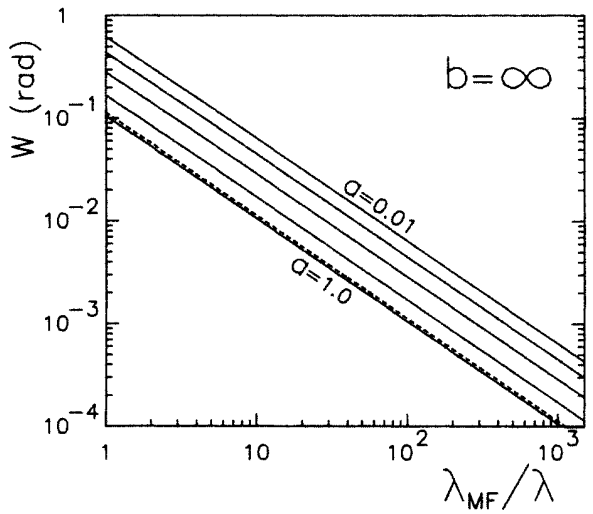

FIG. 11. Full width at half maximum W of the backscattering cone, in the diffusion approximation for a semi-infinite slab ($b=\infty$). Curves are given for five different albedos as a function of λ_{MF}/λ. Also for $a=1$ the exact (extrapolated for $b\rightarrow\infty$) result (dashed line) is given.

approximation for small b is to be expected.

From the point of view of an experimentalist, it is instructive to calculate so-called "difference slabs" (see Ref. 15). Here, the backscattering intensities from two slabs with optical thicknesses b_1 and b_2 are subtracted. In this way, the scattering contributions coming from the front layer ($\tau<b_1$) can be eliminated, and only the contributions of the light that have been in the back end of the slab ($b_1<\tau<b_2$) remain. To be more precise, the backscattering of such a difference slab contains exactly all those lightpaths that have their *deepest point* at an optical depth τ_d, with $b_1<\tau_d<b_2$. Since the number of lightpaths that have their *deepest point* at an optical depth τ_d does not change with the optical thickness b of the sample (at least if $b>\tau_d$), this also holds if that difference slab is situated in the middle of a thicker slab with optical thickness $b>b_2$.

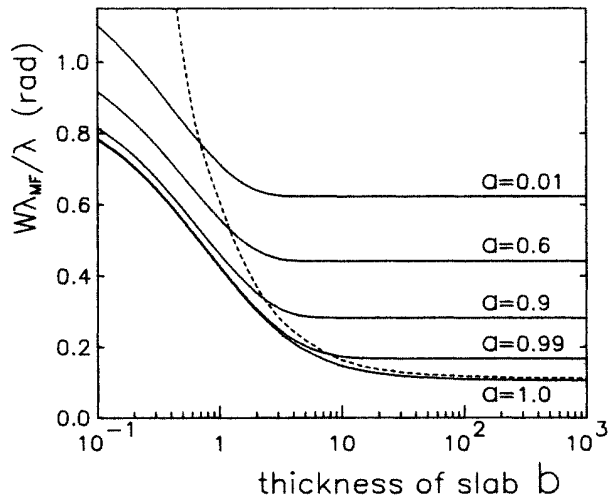

FIG. 12. The value $W(\lambda_{MF}/\lambda)$ is plotted against the optical thickness b. The solid lines give the results from the diffusion approximation for five different values of the albedo. The dashed curve gives the result for the exact theory with $a=1$.

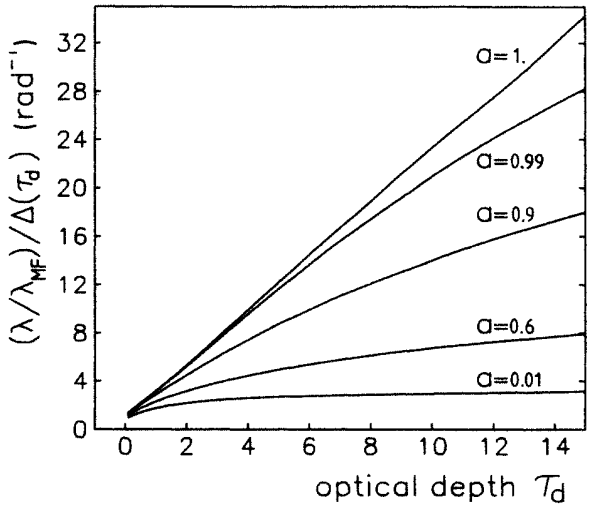

FIG. 13. The value $(\lambda/\lambda_{MF})/\Delta(\tau_d)$, associated with a difference slab of infinitesimal thickness at an optical depth τ_d, is plotted against τ_d for five different values of the albedo a. Notice that for $a=1$ the curve is a straight line which goes through the abscissa at $\tau_d\simeq-0.5$. Experimental results are given in Fig. 21.

The width of the backscattering cone associated with the lightpaths that have their deepest point in the difference slab b_1 to b_2, or $b_1<\tau_d<b_2$, is defined as $W[\gamma_c(b_2)-\gamma_c(b_1)]$, which we can use to define the width Δ of the backscatter cone associated with a difference slab of infinitesimal thickness at the optical depth τ_d:

$$\Delta(\tau_d)\equiv\lim_{b_1\rightarrow b_2} W[\gamma_c(b_2)-\gamma_c(b_1)],\quad b_1<b_2\ . \tag{70}$$

In Fig. 13 this is used to plot the value $(\lambda/\lambda_{MF})/\Delta(\tau_d)$ against τ_d for some values of the albedo a. The figure shows that $\Delta(\tau_d)$ is inversely proportional to the optical depth τ_d in case $a=1$.

It is of interest to analyze the angular dependence of the enhanced backscattering in the neighborhood of the exact backscattering direction. Analysis of $\gamma_{c,\infty}$ near backscattering angle for the albedo close or equal to 1 gives

$$\gamma_{c,\infty}=\tfrac{3}{2}a^2\left[1+2\tau_0-2(\tau_0+1)^2\left[3(1-a)+\frac{k_0^2}{\kappa^2}\theta_s^2\right]^{1/2}\right]$$
$$+O(\theta_s^2)\ , \tag{71}$$

which for $a=1$ gives

$$\gamma_{c,\infty}=\tfrac{3}{2}\left[1+2\tau_0-2\frac{k_0}{\kappa}\,|\,\theta_s\,|\,(\tau_0+1)^2\right]+O(\theta_s^2)\ , \tag{72}$$

which clearly shows that the solution is nonanalytic for $a=1$. So we see, that the top of the backscatter cone is a hyperbola for $a<1$ and a triangle for $a=1$.

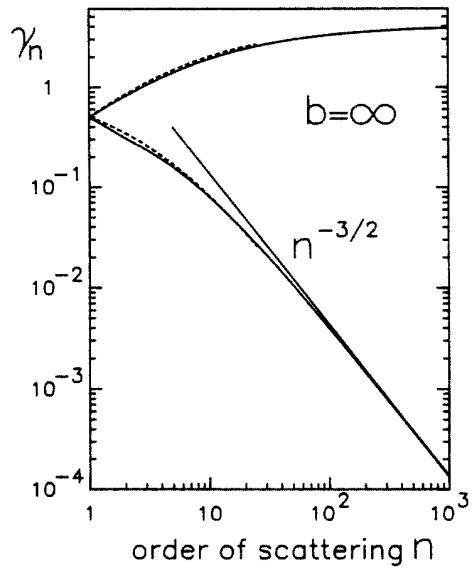

FIG. 14. The nth-order scattering contribution to the total amount of scattering γ in case $b=\infty$, $a=1$, and $\mu_i=\mu_s=1$ for both the exact theory (dotted lines) and the diffusion approximation (solid lines). The convergence of the high-order scattering to the $n^{-3/2}$ asymptote is clear. It is also seen that the lower-order scattering is underestimated by the diffusion approach. The cumulative curve $\sum_n \gamma_n$ is also given. See also Table I.

It would be extremely useful if one could decompose the results of the diffusion theory in a summation of terms in which each term describes the next order of scattering. In such a way the theory could even be tested much better against exact theories. To this end we have to express the diffusion result for the bistatic coefficients in a Taylor series of the albedo. Expansion of (69) in the albedo gives the separate contribution γ_n for each order of scattering for the case $b=\infty$. This can be done by calculating the nth derivative of $\gamma_{c,\infty}$ and substituting $a=0$:

$$\gamma_{c,\infty}=\sum_{n=0}^{\infty}\gamma_n a^n\,, \tag{73a}$$

$$\gamma_{n+2}=\frac{d^n\gamma_{c,\infty}}{n!da^n}\bigg|_{a=0}\,. \tag{73b}$$

The solution is implicitly given by a set of iterative equations

$$\gamma_{n+2}=\frac{3}{2n!}\sum_{m=0}^{n}\frac{\delta_{nm}}{[c(c+1)]^{m+1}}\times\left[A_m-\frac{\exp(-2c\tau_0)}{1+c}B_m\right], \tag{73c}$$

$$A_m=\sum_{k=0}^{m}\alpha_{mk}c^k,\quad \alpha_{00}=1 \tag{73d}$$

$$B_m=\sum_{k=0}^{2m}\beta_{mk}c^k,\quad \beta_{00}=1 \tag{73e}$$

$$\alpha_{mk}=(k-m)\alpha_{m-1,k}+(k-1-2m)\alpha_{m-1,k-1}\,, \tag{73f}$$

TABLE I. The nth-order scattering contribution to the total amount of scattering γ in case $b=\infty$, $a=1$, and $\mu_i=\mu_s=1$ for both the exact theory and the diffusion approximation. It is seen that the lower-order scattering is underestimated by the diffusion approach. The cumulative curves $\sum_n \gamma_n$ are also given. See also Fig. 14.

n	$\gamma_{n,\mathrm{dif}}$	$\gamma_{n,\mathrm{exa}}$	$\sum_n \gamma_{n,\mathrm{dif}}$	$\sum_n \gamma_{n,\mathrm{exa}}$
1	0.5000	0.5000	0.5000	0.5000
2	0.3071	0.3465	0.8071	0.8465
3	0.2356	0.2611	1.0426	1.1076
4	0.1903	0.2066	1.2330	1.3142
5	0.1582	0.1692	1.3912	1.4834
6	0.1343	0.1421	1.5254	1.6254
7	0.1159	0.1214	1.6413	1.7469
8	0.1013	0.1055	1.7426	1.8524
9	0.0896	0.0928	1.8323	1.9452
10	0.0801	0.0825	1.9124	2.0277
∞	0.0000	0.0000	4.1313	4.2277

$$\beta_{mk}=(k-m)\beta_{m-1,k}+(k-2-2m-2\tau_0)\beta_{m-1,k-1}-2\tau_0\,\beta_{m-1,k-2}\,, \tag{73g}$$

$$\delta_{nm}=(n-1-\tfrac{1}{2}m)\delta_{n-1,m}-\frac{c}{2}\delta_{n-1,m-1},\quad \delta_{11}=-\frac{c}{2} \tag{73h}$$

with $\alpha_{m,-1}=\beta_{m,-2}=\beta_{m,-1}=\beta_{m,2m+1}=\beta_{m,2m+2}=\delta_{n,0}=\delta_{n,n+1}=0$ and $c=3^{1/2}$. The results of this expansion are shown in Fig. 14 and Table I. It is seen that only for the very lowest orders of scattering there is some discrepancy between the values for $\gamma_{c,\infty}$ as calculated from the exact theory and the diffusion approximation. This was to be expected since a wave is only propagating diffusively after it has scattered several times. From Fig. 14 it is also seen that the contribution of each order of scattering is proportional to $n^{-3/2}$ for higher-order scattering.

IV. EXPERIMENTAL RESULTS

Detailed data have been collected on (i) the scattering and transport mean free paths λ_{sc} and λ_{tr} (the characteristic lengths associated with the attenuation of the coherent beam and of energy transport) as a function of sample composition, and (ii) the shape and width of the cones of enhanced backscattering as a function of the transport mean free path and the slab thickness d ($\equiv b\lambda_{tr}$).

A. Scattering and transport mean free path

For suspensions of different concentrations of 0.215 μm, 0.482 μm, and 1.019 μm polystyrene spheres, and of 2.02 μm polyvinyltoluene spheres (Dow Chemical) we calculated λ_{sc} and λ_{tr} from Mie theory.[24] For suspensions of surface-treated TiO_2 (rutile) particles in 2-methylpentane-2,4-diol (samples were kindly supplied by Sikkens and by Sigma Coatings) we determined the scattering and

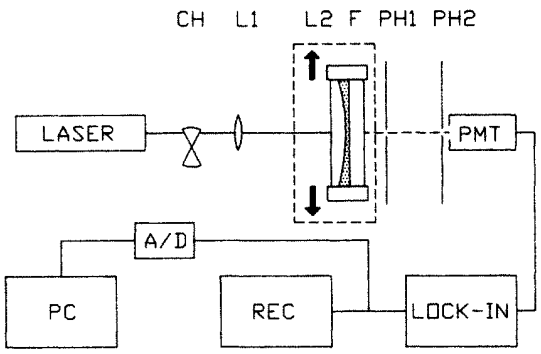

FIG. 15. Scheme of the experimental setup for the observation of transmitted intensity as a function of slab thickness. CH, chopper; $L1$, lens; $L2+F$, cell consisting of a weak lens and an optical flat mounted on a translation stage; PH1 and PH2, pinholes.

transport mean free paths from transmission experiments. Figure 15 shows the setup used for the determination of the transmitted intensity I_t as a function of slab thickness: a laser beam was passed through a weak positive lens $L1$ so as to obtain a long focus with its waist near the pinhole PH1. The cell consisted of another weak positive lens L2 and an optical flat F. Pinhole PH2 was chosen just big enough to make sure that no clipping occurred upon scanning the cell (filled with solvent only) through the beam over its full range. In Fig. 16 a typical curve for transmission versus slab thickness is presented. Three distinct parts can be distinguished: part (a) shows the exponential decay of the transmitted coherent intensity that results from light scattering out of the beam. From its slope, the scattering mean free path λ_{sc} is found. Near point A the diffuse intensity starts to outweigh the coherent intensity, and part (2) shows the $1/d$ decay of the diffuse intensity. In this range a plot of $(V_{out})^{-1}$ (V_{out} being the amplified detector signal) versus d gives a straight line with a slope of $(C\lambda_{tr})^{-1}$, with C an as yet unknown constant of dimensions Volt per length. Near point B the absorption of the sample starts to play a role,

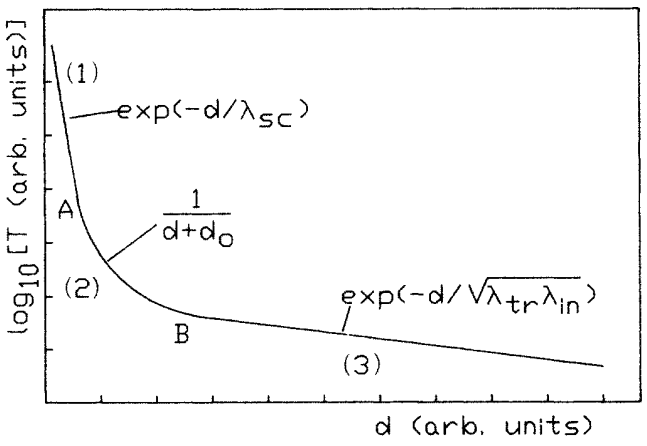

FIG. 16. Typical plot of log(transmission) vs slab thickness. (1), exponential decay of coherent intensity. (2), $1/d$ decay of diffuse intensity (diffusion). (3), exponential decay of diffuse intensity (absorption).

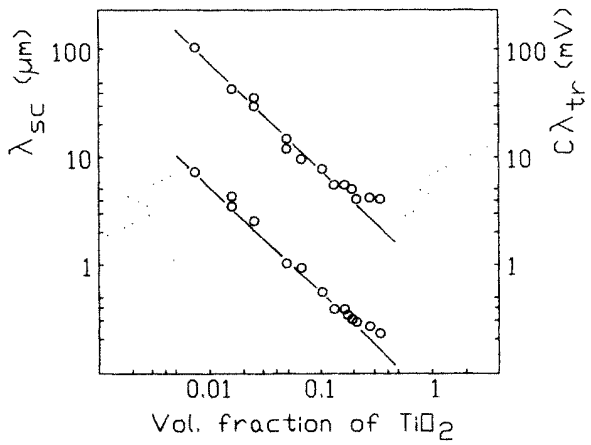

FIG. 17. Scattering mean free path (lower plot) and (upper plot) transport mean free path times a constant (see text) as a function of the volume fraction of $\varnothing \simeq 220$-nm TiO_2 particles.

and in part (3) the decay is once more exponential. From its slope we obtain $(\lambda_{tr}\lambda_{in})^{-1/2}$, where λ_{in} is the inelastic mean free path.

In Fig. 17 the experimental values for λ_{sc} (in μm) and $C\lambda_{tr}$ (in mV) are plotted versus the volume fraction V of TiO_2. For low volume fractions ($V<0.1$) both λ_{sc} and λ_{tr} are inversely proportional to V. At higher concentrations saturation occurs (possibly earlier for λ_{tr} than for λ_{sc}), showing that we are entering the dependent scattering regime. From the upper curve we found λ_{tr} as a function of V in the following way: in the dilute regime, λ_{tr} is known to be equal to $\lambda_{sc}/(1-\langle\cos\theta\rangle)$, with $\langle\cos\theta\rangle$ the average cosine of the scattering angle. The average size of the TiO_2 particles is 220 nm.[44] Assuming spherical shape, Mie theory yields a value of 0.476 for $\langle\cos\theta\rangle$ and hence λ_{tr} should be $\simeq 1.87\lambda_{sc}$. From this result and from the vertical distance between the two plots, the values of the constant C was calculated to be 14.3×10^3 V m^{-1}. Using this value, we can now find λ_{tr} from the upper curve (i.e., from the diffusive $1/d$ decay) *also* for concentrated samples where the proportionality between λ_{sc} and λ_{tr} might no longer hold. (Taking into account that the size distribution of the crystals is wide and that their shape is not spherical, the above procedure cannot be expected to give more than a reasonable estimate of λ_{tr}).

B. Enhanced backscattering

Enhanced backscattering was recorded using a setup of the type drawn schematically in Fig. 18. A linearly polarized laser beam was expanded and then reflected from a beam splitter onto the sample cell. The intensity backscattered through the beamsplitter was recorded as a function of the scattering angle, using a pinhole-detector assembly mounted on a stepper-motor driven translation stage and positioned with the pinhole in the focal plane of the lens L. The cell was tilted off-axis so as to keep its window reflections well away from the detector. In scans of high-viscosity samples the cell was spun around its axis to average out the strong intensity fluctuations that result from interference.[12,14] The transmission characteristics

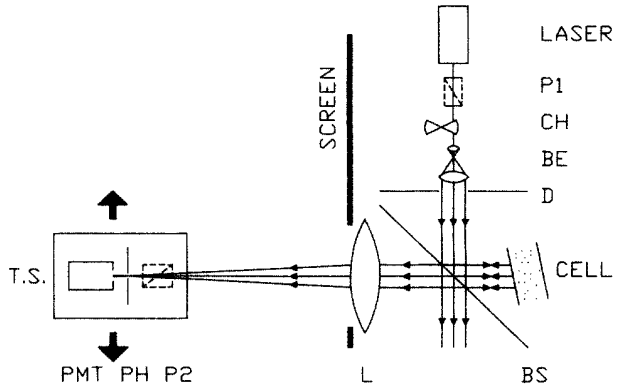

FIG. 18. Experimental setup for the observation of backscattering enhancement. $P1$, $P2$, polarizers; CH, chopper; BE, beam expander; BS, beam splitter; L, lens; PH, pinhole; TS, translation stage.

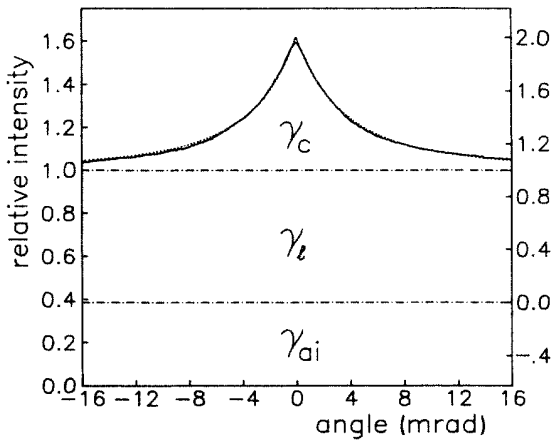

FIG. 19. Enhanced backscattering of the parallel light component from a 2300-μm slab of a 1.05-vol% sample of $\varnothing \simeq 220$ nm particles of TiO_2 in 2-methylpentane-2,4-diol at $\lambda_{vac} = 514.5$ nm. Solid line: experimental curve. Dotted line: curve, calculated from diffusion theory, using $\lambda_{tr} = 9.68$ μm. For practical reasons, the theoretical curve convolved with the instrumental resolution of 0.5 mrad, is not shown. The left-hand vertical axis corresponds to the experimental curve, while the right-hand axis corresponds to the theoretical decomposition in contributions from the ladder terms γ_l, the interference terms γ_c, and the angle-independent terms γ_{ai}.

of the beam splitter depend on the angle of observation and (depending on the extent of the scanning range) measured intensities may need to be corrected for this effect. "Response curves" were obtained illuminating the sample from the backside, i.e., using it as just a diffuse light source. The polystyrene-sphere samples were studied over a total scan width of ≤ 50 mrad. Within this narrow range no corrections for response variations were needed. Dilute TiO_2 samples were studied using a scan width up to 175 mrad. For the more concentrated TiO_2 samples the setup was slightly modified: in terms of Fig. 18, the detector was now moved in a plane perpendicular to the plane of the drawing (making the scan symmetrical with respect to the transmission characteristics of the beam splitter) and along a circular path around the cell. The lens L, which in the narrow-angle scans was at a fixed position, now moved with the detector assembly. The total scan width was 600 mrad. All TiO_2 curves were corrected for the angular dependence of the response.

For a given sample, the recorded *enhancement factor* $I_{top}/I_{background}$ depends on the relative orientation of the polarizers $P1$ and $P2$. The *width* of the cone depends on λ_{tr} and for very small particle samples also on the spatial orientation of the scanning plane with respect to the direction of incident polarization: low-order scattering contributions are then abnormally broad when the cone is scanned in the plane of incident polarization.[15] The present (isotropic) theory is expected to hold for the parallel light component ($P1 \| P2$) and will be compared to experimental results obtained from scans perpendicular to the direction of incident polarization.

The theory takes into account *self-avoiding light paths* (ladder diagrams) and interference between such paths and their time-reversed counterparts (most-crossed diagrams). This leads to a predicted enhancement factor of 2.[5] In the experiment lower values are found. Reported enhancement factors are 1.6,[22] 1.65,[10] 1.70,[11] 1.75,[14] and 2.[12,45] These values suggest that a considerable contribution to the background intensity is due to lightpaths that either have no time-reversed counterpart (e.g., single scattering), or give rise to interference terms that are not angle dependent (we come back to this point at a later stage).

Now even if the isotropic theory would not describe the relative intensities of background and cone fully correct, it might still correctly describe the *shape* and the *width* of the cone, provided that the latter is indeed mainly due to most-crossed-diagram type of interference. In Fig. 19, the backscattering pattern as recorded using a thick slab ($b \simeq 240$) of 1.05 vol% and diameter $\phi \simeq 0.22$ μm rutile particles in 2-methylpentane-2,4-diol as a sample, is plotted together with the intensity profile as calculated for this sample from diffusion theory (this slab thickness is outside the region that can be handled numerically with the exact theory), using the value for λ_{tr} that was obtained from transmission experiments. The theoretical curve was fitted to the experimental data in the following way: the calculated intensity profile was convolved with the instrumental resolution. (The advantage of convolving the calculated curve instead of deconvolving the experimental one is that no assumptions regarding the shape of the latter are needed.) The tops of the resulting theoretical and experimental curves were then superimposed and the vertical scale of the calculated curve was adapted so as to make the outermost parts of its wings coincide with those of the experimental cone. The shape and width of the calculated cone is found to fit perfectly to the experimental data. At the same time we see that the observed intensity profile has an offset with respect to the calculated one that amounts to approximately 30% of the total background. This seems to be far too much to be explained in terms of single scattering by an ideal sample, so another angle-independent scattering contribution must play a part. In Fig. 19, we denoted the bistatic scattering coefficient of all angle-independent (ai) terms (including single scattering) by γ_{ai}. If the sam-

ple thickness is reduced to a few microns only, an essentially flat (no cone) backscattering pattern remains, of which the intensity is still $\simeq 10\%$ of that of the background signal from a thick slab. This remaining intensity is thought to result from two contributions: (i) (near-) forward scattering in combination with reflection from the rear window (because of the inclined position of the cell, its windows cannot reflect the incident beam directly into the detector. *Scattered* light, however, may reach the detector after reflection from the rear window and from the reflected incident beam light may also be scattered into the detector) and (ii) scattering from particles that adhere to the windows (if the solid component of the sample tends to adhere to the glass of the cell windows, a single scattering contribution would result from an ideal sample). In order to minimize the first effect, a black rear window was used with an index of refraction close to that of the sample. If the sample is sufficiently thick, only the second effect remains.

As explained in Sec. III, we used a difference technique to probe the width and the enhancement factor of the contribution to the backscatter cone as a function of the depth in the sample: subtracting the backscattering patterns of slabs of thickness d_1 and d_2 $(d_2 > d_1)$, the scattering contributions coming from the front layer of the sample $(z < d_1)$ cancel out, and what remains is the contribution of light that has "seen" the deeper part of the slab $(d_1 < z < d_2)$. In this way the single scattering contribution (which has no angle-dependent interference term) can be eliminated. It is also possible to exclude the contribution of the very long lightpaths that give rise to the narrow top of the cone by choosing d_2 relatively small.

Figure (20a) shows difference cones that were obtained with this technique, using the sample that gave the full one of Fig. 19. In order to present several curves in the same figure without loosing clarity, a normalization procedure was performed that is more conveniently outlined if we first discuss the corresponding calculated cones. The latter are plotted in Fig. 20b and were obtained in the following way: the intensity profiles were calculated from diffusion theory using experimentally obtained λ_{tr} values, and convolved with the instrumental resolution. The resulting (convoluted) curves were normalized, each with respect to its own background level. We return now to the experimental curves: the vertical scales of the cones in Fig. 20a were adapted so as to match their heights (intensities) to those of their calculated counterparts. The experimental and calculated widths and relative intensities and the experimental enhancement factors for series of difference cones that were recorded using samples with different volume fractions of TiO_2 are listed in Table II. (The values listed for the 1.05 vol % sample correspond to the cones of Fig. 20.)

Comparing the shapes, widths, and relative intensities of the calculated and experimental cones, we find a good general agreement. Comparing the enhancement factors (Table II), we see that in general the experimental values are lower than the predicted value of 2. The cones of the 1.05 vol % sample may serve as an example (for illustrative purposes the—less reliable—front slabs are also

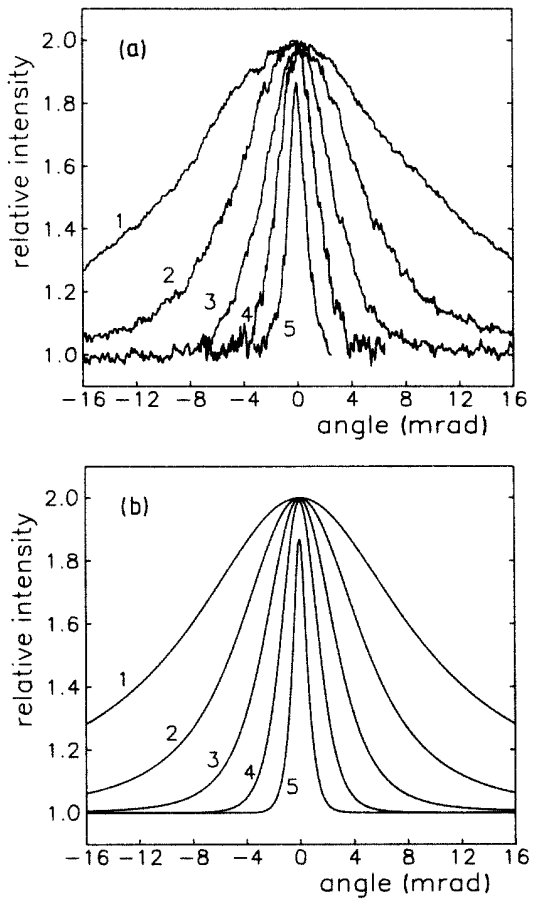

FIG. 20. (a) Normalized (see text) difference cones recorded for the parallel light component using the sample of Fig. 19. Difference slabs: curve 1, 0–13 μm; curve 2, 13–25 μm; curve 3, 25–50 μm; curve 4, 50–100 μm; curve 5, 100–1000 μm. (b) Normalized backscattering curves, calculated from diffusion theory for the difference slabs of (a), using $\lambda_{tr} = 9.68$ μm.

given): in the very front layer the enhancement factor is lowest, and this is thought to be a result of the single scattering contribution. In the next layer, which is the first *difference* slab, a relatively high value is found. To obtain the difference cone associated with this slab, a pattern containing a relatively big contribution via the rear window (see before) is subtracted from one in which this contribution is attenuated by passing through a thicker slab. As a consequence the background of the resulting difference cone is too low, and the corresponding enhancement factor is too high. For deeper difference slabs, the enhancement factor seems to become constant. We have reported earlier on difference cones that were recorded using polystyrene spheres in water.[15] In that study we found an enhancement factor near 2 for a difference slab of two slabs with optical thickness $b_1 = 0.6$ and $b_2 = 1.8$. On the basis of our present results we believe that the effect of the rear window may have played a part there and that the real factor is probably lower.

It remains to be explained why the experimental enhancement factors found are smaller than 2. Single scattering contributions cannot be expected to be of importance in the backscattering patterns from deep slabs.

TABLE II. Experimental values for width, relative intensity, and enhancement factor, and values calculated for width and relative intensities from diffusion theory for difference slabs as a function of λ_{tr} and optical depth. Relative intensities were normalized with respect to the total intensities of the difference slabs given for each sample.

Concentration (vol %)	λ_{tr} (μm)	Optical depth (τ_d)	$\Delta(\tau_d)$ Expt.	$\Delta(\tau_d)$ Calc.	Relative intensity Expt.	Relative intensity Calc.	Enhancement factor (Expt.)
0.36	28.2	0.35–0.9	7.8	7.5	0.09	0.13	2.0
		0.9–1.6	4.6	5.0	0.26	0.19	1.83
		1.6–4.6	2.4	2.6	0.45	0.46	1.69
		4.6–8.9	1.1	1.2	0.21	0.22	1.60
1.05	9.68	0.0–1.3	21.	20.	0.24	0.22	1.38
		1.3–2.6	10.3	10.4	0.21	0.21	1.87
		2.6–5.2	5.4	5.9	0.21	0.23	1.71
		5.2–10.3	3.1	3.1	0.17	0.17	1.69
		10.3–103.0	1.2	1.1	0.16	0.17	1.65
2.50	4.06	2.0–6.1	17.0	15.0	0.54	0.57	1.71
		6.1–9.8	8.0	7.0	0.17	0.17	1.63
		9.8–49.1	3.9	3.0	0.28	0.27	1.61
9.81	1.04	5.8–12.5	29.0	25.0	0.53	0.56	1.67
		12.5–24.0	15.0	13.0	0.21	0.27	1.54
		24.0–48.0	7.9	6.8	0.26	0.16	1.65

Lightpaths that return to their starting point (loops) would contribute angle-independent interference terms and therefore also apparently reduce the enhancement factor. However, we would expect the relative contribution of loops to decrease with increasing order of scattering.

From Fig. 20 and Table II it is obvious that the deeper a difference slab is situated in the sample, the narrower its contribution to the cone. The width of such a contribution is inversely proportional to the average distance between both ends of the lightpaths associated with the difference slab. Those lightpaths have in common that their deepest point is situated in that difference slab. Since the light performs a random walk, the average distance between the ends of a lightpath will be proportional to the greatest depth of that lightpath, which explains why the deeper a difference slab is situated in the sample, the narrower its contribution to the cone indeed.

Classes of lightpaths that traveled to the same *optical* depth τ_d in media with different λ_{MF} are expected to yield contributions to their respective cones of which the width relate as λ_{MF}^{-1}. In Fig. 21 we have plotted values of $(\lambda/\lambda_{MF})/\Delta(\bar{\tau}_d)$ as found for series of difference cones from four different concentrations of TiO_2 suspensions versus $\bar{\tau}_d$ (where $\bar{\tau}_d$ is the average value of the optical thicknesses b_2 and b_1 of the subtracted slabs). The relationship between the two quantities was also evaluated from diffusion theory (cf. Fig. 13) and for albedo $a=1$

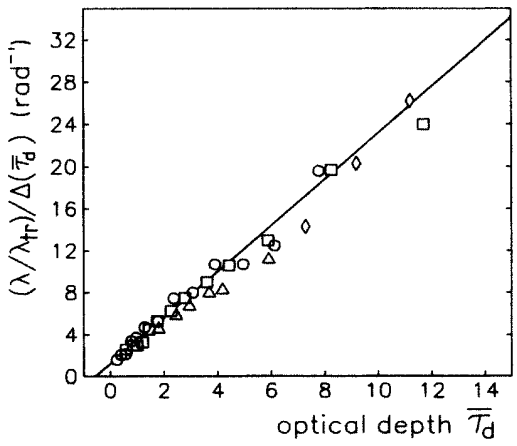

FIG. 21. $(\lambda/\lambda_{tr})/\Delta(\bar{\tau}_d)$ vs $\bar{\tau}_d$ for difference slabs in samples of different volume fractions of TiO_2 particles in 2-methylpentane-2, 4-diol. ○, 0.36 vol %; □, 1.05 vol %; △, 2.50 vol %; ◇, 9.81 vol %. Solid line: $(\lambda/\lambda_{tr})/\Delta(\bar{\tau}_d)=2.2(\bar{\tau}_d+0.5)$. See also Fig. 13.

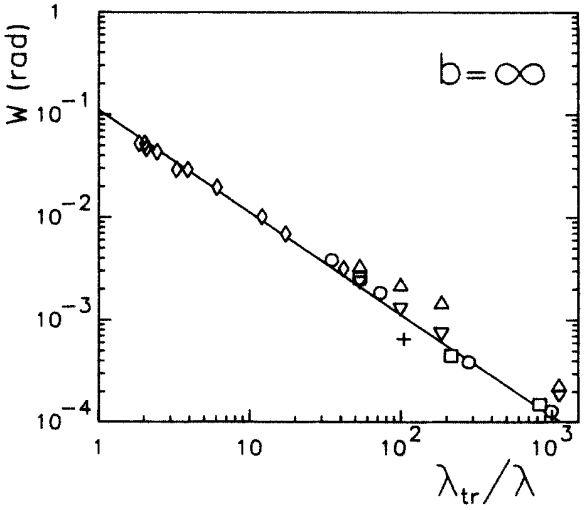

FIG. 22. Full width W of the cone of enhanced backscattering vs λ_{tr}/λ for very thick slabs. ◇, 0.22-μm TiO_2 in 2-methylpentane-2,4-diol; ○, 1.091-μm polystyrene spheres in water; □, 0.482-μm polystyrene spheres in water; △, 0.214-μm polystyrene spheres in water (∥ scan); ▽, 0.214-μm polystyrene spheres in water (⊥ scan); +, 2.02-μm polyvinyltoluene spheres in water. Solid line: $W=(0.7/2\pi)(\lambda_{tr}/\lambda)$, the extrapolated result from the exact theory for $b=\infty$.

the result may be fitted as $(\lambda/\lambda_{MF})/\Delta(\bar{\tau}_d)\simeq 2.2(\bar{\tau}_d+0.5)$. This relationship is shown in Fig. 21 as a continuous line. Good agreement with experiment is once more found. From Fig. 21 we conclude that the width $\Delta(\bar{\tau}_d)$ of the contribution to the cone by a difference slab at depth d is proportional to $(d+\lambda_{MF}/2)^{-1}$ or, essentially independent of λ_{MF} once $d \gg \lambda_{MF}$.

In Fig. 22 experimental width W for complete cones of enhanced backscattering as measured for the light component polarized parallel to the incident beam are plotted versus $\lambda_{tr}/\lambda_{medium}$. Our exact isotropic theory predicts that the two quantities should relate as

$$W \simeq \frac{0.7}{2\pi}(\lambda/\lambda_{tr}) .$$

This relationship is represented in Fig. 22 by a solid line.

ACKNOWLEDGMENT

This work is part of the research program of the "Stichting voor Fundamenteel Onderzoek der Materie" (FOM), which is financially supported by the "Nederlandse Organisatie voor Zuiver-Wetenschappelijk Onderzoek" (ZWO). The authors wish to thank Dr. R. Hond of Sigma Coatings and Mr. J. H. Franssen of Sikkens B.V. for kindly supplying TiO_2 samples.

APPENDIX A

To calculate the kernel $W(\tau,\alpha)$, it appears convenient to make a linear interpolation table $W(I,J)$ of $W(\tau,\alpha)$. Because $W(\tau,\alpha)$ diverges for $\tau\to 0$ as $-\ln(\tau)$, we need more interpolation points for small τ, proportional to $1/\tau$, the derivative of $-\ln(\tau)$. This is achieved by mapping τ on I^2 instead of I, starting at a value $\tau_0=10^{-5}$. Similarly, α was mapped on J^2 in order to get a smooth picture of the backscattering cone. Integration was done with an adaptive Gaussian quadrature.[46] In order to avoid problems for higher values of t due to the disproportion of the length of the interval Δt and its contribution to the integral, the integration interval $[1,\infty)$ was mapped on $[0,1)$ by use of the conform map

$$t=\frac{1+\xi}{1-\xi} , \tag{A1}$$

so

$$W(\tau,\alpha)=\int_1^\infty \frac{\exp[-\tau(t^2+\alpha^2)^{1/2}]}{(t^2+\alpha^2)^{1/2}}dt$$

$$=2\int_0^1 \frac{\exp[-\tau\eta(\xi,\alpha)/(1-\xi)]}{(1-\xi)\eta(\xi,\alpha)}d\xi , \tag{A2}$$

and

$$\eta(\xi,\alpha)=[\alpha^2(1-\xi)^2+(1+\xi)^2]^{1/2} . \tag{A3}$$

APPENDIX B

To calculate the different orders of scattering with Eqs. (48) and (49) it is important to separate the integration interval in two parts chosen so that the singularity of the kernel is in the boundary. The kernel occurs twice for third-order scattering, and this means we have to split the interval $[0,b]$ in three parts, namely $[0,\tau_1)$, (τ_1,τ_2), and $(\tau_2,b]$ for $\tau_2>\tau_1$, because here we have to avoid both singularities. Due to this complication Γ_3 rather than Γ_2 should be used as the starting term for iteration.

APPENDIX C

The integral equation we have to solve is a Fredholm equation with a singular kernel $W(\tau,\alpha)$.[39] In order to calculate the solution of (30) numerically, we have to discretize the continuous variable τ. Divide the interval $[0,b]$ in N parts so $\tau_n=bn/N$ and (33) becomes

$$\Gamma(\tau_n,\tau_l;\alpha)=S(\tau_n,\tau_l;\alpha)+\frac{a}{2}\sum_{m=0}^{N-1}\int_{t_m}^{t_{m+1}} W(|\tau_n-\tau|;\alpha)\times\Gamma(\tau,\tau_l;\alpha)d\tau . \tag{C1}$$

Linear interpolation of Γ between τ_m and τ_{m+1} with $\tau=\tau_m+t$ gives

$$\Gamma(\tau_m+t,\tau;\alpha)=\frac{t\Gamma(\tau_{m+1},\tau;\alpha)+(\tau_{m+1}-\tau_m-t)\Gamma(\tau_m,\tau;\alpha)}{\tau_{m+1}-\tau_m} , \tag{C2}$$

So with Eqs. (C1), (C2), and $x=tN/b$, and the definitions

$$\Gamma(\tau_n,\tau_l;\alpha)\equiv\Gamma_{nl}(\alpha) , \tag{C3a}$$

$$S(\tau_n,\tau_l;\alpha)\equiv S_{nl}(\alpha) , \tag{C3b}$$

we find

$$\Gamma_{nl}(\alpha)=S_{nl}(\alpha)+\frac{ab}{2N}\sum_{m=0}^{N-1}\int_0^1 W\left(\left|\frac{b}{N}(n-m-x)\right|;\alpha\right)[x\Gamma_{m+1,l}(\alpha)+(1-x)\Gamma_{ml}(\alpha)]dx , \tag{C4}$$

which gives

$$\Gamma_{nl}(\alpha)=S_{nl}(\alpha)+\frac{ab}{2N}\Gamma_{0l}(\alpha)\int_0^1 xW\left(\left|\frac{b}{N}(n-1+x)\right|;\alpha\right)dx+\frac{ab}{2N}\Gamma_{Nl}(\alpha)\int_0^1 xW\left(\left|\frac{b}{N}(n+1-N-x)\right|;\alpha\right)dx$$
$$+\frac{ab}{2N}\sum_{m=1}^{N-1}\Gamma_{ml}(\alpha)\int_0^1 x\left[W\left(\left|\frac{b}{N}(n-m-1+x)\right|;\alpha\right)+W\left(\left|\frac{b}{N}(n-m+1-x)\right|;\alpha\right)\right]dx . \tag{C5}$$

This can be written as

$$\Gamma_{nl}(\alpha)=S_{nl}(\alpha)+C_{nm}(\alpha)\Gamma_{ml}(\alpha) ,$$

so that

$$\Gamma_{ml}(\alpha)=[\delta_{mn}-C_{mn}(\alpha)]^{-1}S_{nl}(\alpha) . \tag{C6}$$

To find the solution we have to calculate the inverse of the $(N+1)(N+1)$ matrix $[\delta_{mn}-C_{mn}(\alpha)]$. A larger N results in a more accurate solution, but CPU time increases with about N^3. On a VAX 11/750 slabs up to $b=32$ could be handled this way. Γ_3 or a higher-order scattering solution should be used as a starting term to avoid the unboundness of Γ_2.[46]

[1]S. John and M. J. Stephen, Phys. Rev. B **28**, 6358 (1983).

[2]S. John, Phys. Rev. Lett. **53**, 2169 (1984).

[3]T. R. Kirkpatrick, Phys. Rev. B **31**, 5746 (1985); C. A. Condat and T. R. Kirkpatrick, Phys. Rev. Lett. **58**, 226 (1987).

[4]P. W. Anderson, Philos. Mag. B **52**, 505 (1985).

[5]E. Akkermans and R. Maynard, J. Phys. (Paris) Lett. **46**, L1045 (1985).

[6]S. M. Cohen and J. Machta, Phys. Rev. Lett. **54**, 2242 (1985).

[7]P. Sheng and Z. Q. Zhang, Phys. Rev. Lett. **57**, 1879 (1986).

[8]K. Arya, Z. B. Su, and J. L. Birman, Phys. Rev. Lett. **57**, 2725 (1986).

[9]S. Das Sarma, A. Kobayashi, and R. E. Prange, Phys. Rev. Lett. **56**, 1280 (1986).

[10]M. P. van Albada and A. Lagendijk, Phys. Rev. Lett. **55**, 2692 (1985).

[11]P. E. Wolf and G. Maret, Phys. Rev. Lett. **55**, 2696 (1985).

[12]S. Etemad, R. Thompson, and M. J. Andrejco, Phys. Rev. Lett. **57**, 575 (1986).

[13]A. Lagendijk, M. P. van Albada, and M. B. van der Mark, Physica **140A**, 183 (1986).

[14]M. Kaveh, M. Rosenbluh, I. Edrei, and I. Freund, Phys. Rev. Lett. **57**, 2049 (1986).

[15]M. P. van Albada, M. B. van der Mark, and A. Lagendijk, Phys. Rev. Lett. **58**, 361 (1987).

[16]L. Tsang and A. Ishimaru, J. Opt. Soc. Am. A **1**, 836 (1984); **2**, 1331 (1985); **2**, 2187 (1985).

[17]E. Akkermans, P. E. Wolf, and R. Maynard, Phys. Rev. Lett. **56**, 1471 (1986).

[18]A. D. Stone, Phys. Rev. Lett. **54**, 2692 (1985).

[19]P. A. Lee and A. D. Stone, Phys. Rev. Lett. **55**, 1622 (1985).

[20]B. Shapiro, Phys. Rev. Lett. **57**, 2168 (1986).

[21]S. Chandrasekhar, *Radiative Transfer* (Dover, New York, 1960).

[22]W. W. Montgomery and R. H. Kohl, Opt. Lett. **5**, 546 (1980).

[23]T. S. Trowbridge, J. Opt. Soc. Am. **68**, 1225 (1978).

[24]H. C. van de Hulst, *Light Scattering by Small Particles* (Dover, New York, 1981).

[25]C. F. Bohren and D. R. Huffman, *Absorption and Scattering of Light by Small Particles* (Wiley, New York, 1983).

[26]A. Ishimaru, *Wave Propagation and Scattering in Random Media* (Academic, New York, 1978), Vols. I and II.

[27]H. C. van de Hulst, *Multiple Light Scattering* (Academic, New York, 1980), Vols. I and II.

[28]*Multiple Scattering and Waves in Random Media,* edited by P. L. Chow, W. E. Kohler, and G. C. Papanicolaou (North-Holland, Amsterdam, 1981).

[29]M. J. Stephen and G. Cwilich, Phys. Rev. B **34**, 7564 (1986).

[30]U. Frisch, in *Probabilistic Methods in Applied Mathematics,* edited by A. T. Barucha-Reid (Academic, New York, 1968), Vol. I, p. 76.

[31]*Light Scattering by Irregularly Shaped Particles,* edited by D. W. Schuerman (Plenum, New York, 1979).

[32]V. Twersky, J. Opt. Soc. Am. **65**, 524 (1975); L. Tsang, J. A. Kong, and T. Habashy, J. Acoust. Soc. Am. **71**, 552 (1982).

[33]A. Ishimaru and Y. Kuga, J. Opt. Soc. Am. **72**, 1317 (1982).

[34]D. Vollhardt and P. Wölfle, Phys. Rev. B **22**, 4666 (1980).

[35]G. Bergmann, Phys. Rep. **107**, 1 (1984).

[36]W. Götze, J. Phys. C **12**, 1279 (1979); W. Götze, Philos. Mag. B **43**, 219 (1981).

[37]Here we use a much simpler approach than that used in Ref. 16. The approach here can be found in, for instance, Ref. 35.

[38]*Handbook of Mathematical Functions,* edited by M. Abramowitz and I. A. Stegun (Dover, New York, 1972).

[39]K. E. Atkinson, *A Survey of Numerical Methods for the Solution of Fredholm Integral Equations of the Second Kind* (Society for Industrial and Applied Mathematics, Philadelphia, 1976).

[40]H. H. Kagiwada, R. Kalaba, and S. Ueno, *Multiple Scattering Processes* (Addison-Wesley, Reading, 1975).

[41]I. S. Gradshteyn and I. M. Ryzhik, *Table of Integrals, Series, and Products* (Academic, New York, 1980).

[42]A. A. Golubentsev, Zh. Eksp. Teor. Fiz. **86**, 47 (1984) [Sov. Phys.—JETP **59**, 26 (1984)].

[43]M. N Barber and B. W. Ninham, *Random and Restricted Walks* (Gordon and Breach, New York, 1970).

[44]W. A. Kampfer, *Pigment Handbook* (Wiley, New York, 1973), Vol. I.

[45]In the experiments described in Ref. 12 an optical isolator was used to exclude the single scattering contribution. Figure (2.b) in Ref. 12 shows an enhancement factor of $\simeq 1.8$.

[46]Numerical routines were used from the CERN library.